ROYAL SOCIETY OF CHEMISTRY

REVIEW

Check for updates

Dynamic coordination bonding in metal–organic frameworks: fundamental concepts and emerging applications

Sun Ho Park, [ID] †[a] Byong June Kim, [ID] †[a] Jaehyeuk Choi, [ID] [a] Inhoo Kim [ID] [a] and Nak Cheon Jeong [ID] *[ab]

Metal–organic frameworks (MOFs) have long been regarded as rigid crystalline solids with static coordination bonds. Mounting spectroscopic and crystallographic evidence, however, shows that these bonds are dynamic, undergoing transient dissociation and reassociation without loss of framework integrity. This recognition has catalyzed the concept of dynamic coordination bonding, offering a fresh perspective on MOF chemistry and function. In this review, we define this concept and organize it into two complementary modes: (i) metal–guest dynamics at open metal sites and (ii) metal–linker dynamics within the lattice. We combine experimental and theoretical evidence demonstrating that bond dynamics underpin key functions—including non-thermal activation, gas adsorption, heterogeneous catalysis, and the formation of liquid and glassy MOFs. By integrating mechanistic insight with application-level performance, we establish dynamic bonding as a central design principle for MOFs and outline practical levers—metal identity, linker electronics and sterics, pore architecture, and crystal dimension—to tune equilibrium populations. Framed in this way, MOFs emerge not as static scaffolds but as responsive coordination networks, enabling next-generation advances in catalysis, gas storage and separations, and energy-relevant processes.

1 Introduction

Metal–organic frameworks (MOFs) are crystalline porous materials constructed from metal nodes and multitopic organic linkers through coordination bonding. Owing to their permanent porosity, modular topology, and exceptional chemical diversity—which collectively translate into tunable physicochemical properties—MOFs have attracted considerable attention for a broad range of applications, including gas storage and separation,[1–4] catalysis,[5–9] conductivity,[10–13] chemical sensing,[13–16] and atmospheric water harvesting.[17–20] Meanwhile, MOFs have often been regarded as rigid frameworks in which the coordination bonds between metal centers and guest molecules, as well as those between metals and linkers, were presumed to be static and robust.[21,22] This conventional view was instrumental in establishing the foundation of reticular chemistry, enabling the rational design of predictable structures and functions.[23,24]

As the field evolved, however, an increasing number of observations emerged that could not be fully rationalized within the paradigm of static coordination. For instance, phenomena such as post-synthetic metal or linker exchange,[25,26] catalytic

reactivity occurring at coordinatively saturated metal centers,[27–31] and reversible guest exchange at open metal sites (OMSs)[32–37] all reveal that coordination environments in MOFs are intrinsically dynamic. These discoveries indicate that MOFs—despite their crystalline order—should not be viewed as rigid architectures but as dynamic systems in which coordination bonds can undergo rapid and reversible dissociation and reassociation. Recently, recognition of this behavior has prompted a paradigm shift, giving rise to an emerging concept of dynamic coordination bonding nature.

Dynamic coordination bonding refers to a state in which coordination bonds undergo continuous, transient dissociation–association events, thereby allowing structural or chemical reorganization without the collapse of the framework. In MOFs, this dynamicity can be classified into two fundamental categories: (i) metal–guest molecule dynamic bonding occurring at the OMSs and (ii) metal–linker dynamic bonding occurring within the framework lattice (Fig. 1a).

Metal–guest molecule dynamic bonding arises when Lewis-base molecules reversibly coordinate to, and dissociate from, OMSs (Fig. 1b). Spectroscopic and crystallographic analyses—such as Raman spectroscopy, ^{1}H nuclear magnetic resonance (NMR), and single-crystal X-ray diffraction (SCXRD)—provide direct evidence for this reversible coordination by capturing transient association and dissociation processes at the OMSs of paddlewheel nodes. This dynamic process plays a pivotal role in

[a]*Department of Physics & Chemistry, DGIST, Daegu 42988, Korea. E-mail: nc@dgist.ac.kr*
[b]*Center for Basic Science, DGIST, Daegu 42988, Korea*
† These authors contributed equally to this work.

9088 | *J. Mater. Chem. A*, 2026, **14**, 9088–9114

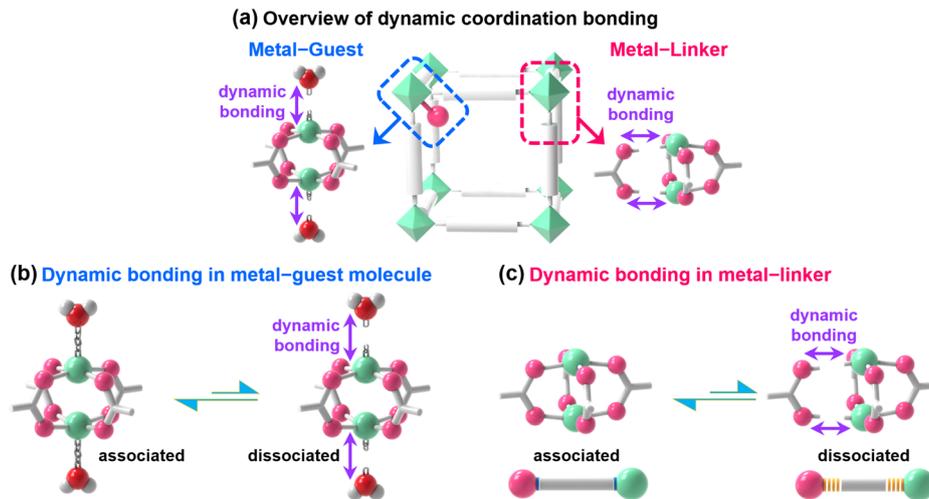This journal is © The Royal Society of Chemistry 2026

Fig. 1 Schematic illustrations of dynamic coordination bonding in MOFs: (a) an overview distinguishing metal–guest dynamics at open metal sites (OMSs) and metal–linker dynamics within the lattice; (b) reversible association–dissociation of Lewis-basic guests at OMSs; (c) transient weakening/cleavage of metal–linker bonds within the framework that generates short-lived open sites (hemilabile states). Purple double arrows denote reversible bond dynamics.

key applications, including framework activation,[33–40] gas adsorption,[41–44] and catalysis[32] among others.

Conversely, metal–linker dynamic bonding involves the transient weakening or partial cleavage of coordination bonds between metal nodes and organic linkers within the framework (Fig. 1c). Variable-temperature vibrational spectroscopy, photoexcitation experiments, and theoretical simulations have demonstrated that these bonds can reversibly transition between associated and dissociated states in response to external stimuli. Such dynamicity underpins a range of intriguing phenomena and functionalities, including catalytic transformations,[45–47] the formation of MOF liquids and glasses,[48–50] and guest-responsive adsorption behavior.[47,51–53]

In this review, we present a comprehensive overview of the dynamic nature of coordination bonding in MOFs, emphasizing the spectroscopic evidence that substantiates its existence. We first describe the fundamental characteristics of metal–guest and metal–linker dynamics, highlighting experimental and theoretical insights that reveal their mechanistic roles in MOF chemistry. We then discuss how these dynamic processes translate into functional applications, including MOF activation, gas adsorption, MOF glass formation, and catalysis. By integrating mechanistic understanding with emerging applications, this review aims to establish dynamic coordination bonding as a unifying principle for the next generation of MOF design and utilization.

2 Dynamicity of metal–guest molecule coordination bonding

OMSs play a crucial role in potential applications of MOFs,[54] although their dynamic coordination bonding nature has rarely been studied. Metal–guest molecule dynamic coordination bonding refers to the instantaneous reversible association and dissociation of Lewis-base molecules at OMSs. In this dynamic state, the coordinative equilibrium is governed by three primary factors: coordination strength, spatial confinedness within the pore, and external stimuli. This section discusses the dynamic behavior of guest coordination at OMSs in terms of (2.1) weak coordination, coordination exchange, and (2.2) laser-induced guest molecule dissociation. Notably, dichloromethane (DCM) and trichloromethane (TCM)—typically regarded as non-coordinating molecules—exhibit weak yet reversible coordination under molecular-scale confinement, indicating an equilibrium between associated and dissociated states. Coordination exchange further reveals that even strongly coordinating molecules can be replaced by weaker ones under ambient conditions, mediated by transient dissociation and reassociation events at OMSs. Moreover, external stimuli such as laser irradiation can induce dissociation through non-radiative thermal relaxation at Cu(II) paddlewheel nodes, underscoring the inherently equilibrium-driven nature of dynamic bonding.

2.1 Dynamic weak coordination bonding and coordination exchange

Dynamic coordination of guest molecules at the OMSs of HKUST-1 arises through instantaneous and reversible association and dissociation under confined conditions. In this section, we describe that weakly coordinating DCM and TCM with low polarity exhibit dynamic equilibrium in their coordination bonds and exchangeability to replace more strongly coordinating molecules such as H_2O, MeOH, EtOH, and MeCN at the OMSs.

2.1.1 Dynamic weak coordination bonding of DCM and TCM within MOF pores. DCM and TCM are conventionally categorized as non-coordinating molecules due to their chemical inertness.[55–59] However, given the primitive assumption that DCM and TCM are weak Lewis bases with lone-paired electrons despite their low polarity, both molecules can act as donors to

This journal is © The Royal Society of Chemistry 2026

J. Mater. Chem. A, 2026, **14**, 9088–9114 | **9089**

metal ions. Nevertheless, due to their extremely low polarity and weak donor strength, DCM and TCM predominantly exist in isolated forms in the bulk liquid phase, making their coordination behavior difficult to characterize using conventional analytical methods.[60] Recently, the Jeong group demonstrated that DCM and TCM can coordinate to metal centers in MOFs in a spatially confined environment. The restricted molecular motion within the nanoscale voids shifts the coordination equilibrium toward the associated state.

To probe this behavior,[32] Cu(II)-based HKUST-1 was chosen as a model system. HKUST-1, constructed from paddlewheel Cu(II) nodes and BTC^{3-} (benzene-1,3,5-tricarboxylate) linkers, features a three-dimensional porous framework composed of two types of large cages (types 1 and 2) and one smaller truncated octahedral cage (type 3). Each Cu(II) center coordinates to four carboxylate oxygen atoms from BTC^{3-} linkers to form a single four-membered ring. Two single four-membered rings link together to form a double four-membered ring, each containing a Cu–Cu paddlewheel node with OMSs oriented toward the large type 1 pore (Fig. 2a). HKUST-1 is particularly well suited for this study because (i) it possesses a high concentration of OMSs; (ii) all OMSs face type 1 open pores accessible to guest molecules; (iii) its large window size (10.5 Å) facilitates guest molecule diffusion and coordination; (iv) its confined nanospace restricts DCM and TCM motion, favoring association; and (v) the paddlewheel Cu–Cu node is Raman-active, displaying a characteristic stretching vibration in the range of 170–230 cm^{-1} that sensitively reflects coordination strength.

On the basis of these considerations, Raman spectroscopic analyses were performed on HKUST-1 samples coordinated with water (H_2O), methanol (MeOH), ethanol (EtOH), acetonitrile (MeCN), N,N-dimethylformamide (DMF), phenol (PhOH), DCM, and TCM—hereafter denoted as H_2O-HK, MeOH-HK, EtOH-HK, MeCN-HK, DMF-HK, PhOH-HK, DCM-HK, and TCM-HK, respectively, where HK refers to fully desolvated HKUST-1. Strongly coordinating molecules such as H_2O, MeOH, EtOH, MeCN, DMF, and PhOH induced substantial red-shifts in the Cu–Cu stretching vibrational band (174–186 cm^{-1}), whereas the coordination-free state exhibited a vibrational mode at 230 cm^{-1}. By contrast, DCM and TCM exhibited intermediate vibrational modes (215 and 218 cm^{-1}, respectively), signifying weak coordination (Fig. 2b). According to Badger's rule,[61] which correlates bond strength with vibrational frequency, weaker coordination results in frequencies closer to the uncoordinated value. The small difference between DCM and TCM further indicates that the coordination strength of TCM is weaker than that of DCM, demonstrating a decrease in coordination strength with an increasing number of neutral chlorine atoms.

To substantiate TCM coordination, SCXRD measurements were performed on both water-included and water-excluded TCM-HK crystals. The former exhibited a shorter Cu–O bond length of 2.184 Å due to H_2O coordination at the OMSs, whereas the latter showed an elongated Cu–Cl distance of 2.385 Å, consistent with TCM coordination at the OMSs.[32] The elongation arises from (i) the larger atomic radius of chlorine compared to oxygen and (ii) the intrinsically weaker donor ability of neutral chlorine atoms compared to oxygen.
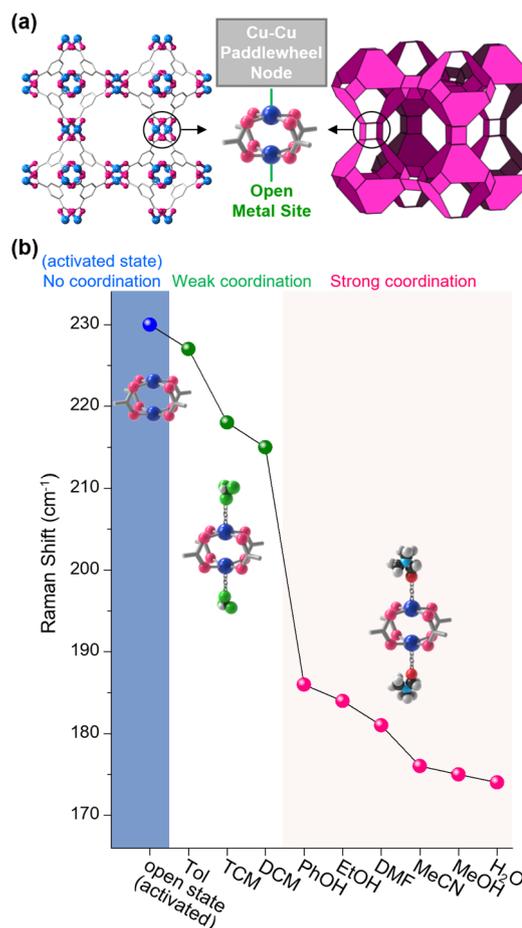

Fig. 2 (a) Structure of HKUST-1 highlighting the Cu–Cu paddlewheel node with an OMS. (b) Raman shift of the Cu–Cu stretching vibration for Act-HK, Tol-HK, TCM-HK, DCM-HK, PhOH-HK, EtOH-HK, DMF-HK, MeCN-HK, MeOH-HK, and H_2O-HK, showing the progression from no coordination (blue) through weak (green) to strong coordination (pink). Reproduced with permission from ref. 32, Copyright 2022, Royal Society of Chemistry.

DFT calculation for the interaction energy between Cu(II) and DCM molecule further demonstrates that the DCM coordination is very weak and thus highly reversible.[39] Specifically, the DFT results show that DCM coordination exhibits an interaction energy of −1.2 kcal mol^{-1}, which is ten times smaller than the energy of strong coordination of e.g., H_2O (−12.5 kcal mol^{-1}), MeCN (−16.4 kcal mol^{-1}), and DMF (−18.5 kcal mol^{-1}). This calculation agreed well with the Cu–Cu vibrational mode in Raman spectroscopy, showing the smaller red shift (215 cm^{-1}) of DCM's weak coordination compared to such strong coordinations (174–186 cm^{-1}) from the coordination-free state of Cu(II) (230 cm^{-1}).

Together, Raman spectroscopy, SCXRD analyses, and DFT calculation confirm the existence of weak coordination bonding of neutral chlorine atoms in DCM and TCM. While these molecules remain non-coordinating in the bulk phase, they exhibit weak yet reversible coordination within the pores of MOFs. This confinement-induced equilibrium shift—rather than the creation of a new bonding mode—highlights the
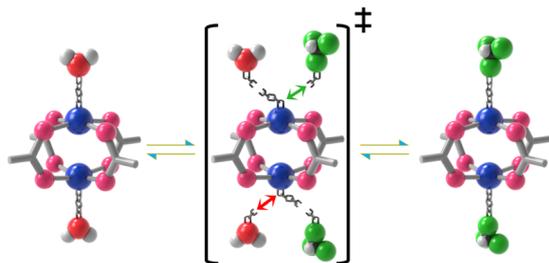
9090 | J. Mater. Chem. A, 2026, 14, 9088–9114

This journal is © The Royal Society of Chemistry 2026

Fig. 3 Schematic illustration of dynamic coordination exchange between H_2O and TCM at a Cu(II) paddlewheel OMS; transient H_2O dissociation enables TCM association, establishing a reversible equilibrium (bracketed species denotes the activated encounter complex). Reproduced with permission from ref. 32, Copyright 2022, Royal Society of Chemistry.

inherently dynamic nature of the process. In a confined environment, chlorine atoms exist in a rapid equilibrium between coordinated and uncoordinated states at OMSs. Thus, weak coordination bonding serves as a prototypical example of dynamic coordination behavior.

2.1.2 Dynamic coordination exchange with weakly coordinating molecules. Coordination exchange at OMSs offers direct experimental evidence for dynamic bonding. In a static bonding model, strongly coordinating molecules would remain permanently attached to metal centers, precluding their substitution by weaker donors. However, experimental studies have revealed that even strongly coordinating molecules can be reversibly replaced by weakly coordinating ones under confined conditions (Fig. 3).
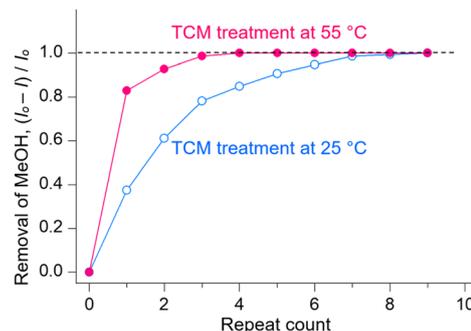

Fig. 5 Removal of MeOH from MeOH-HK as a function of the number of TCM treatments at 25 °C (blue) and 55 °C (red). The fraction removed, $(I_O - I)/I_O$, increases more rapidly at elevated temperature, evidencing thermally accelerated coordination exchange. Reproduced with permission from ref. 35, Copyright 2018, American Chemical Society.

In 2015, Jeong and coworkers provided the first experimental evidence that DCM can replace strongly coordinating molecules at the OMSs.[33] Pristine HK, EtOH-HK, MeOH-HK, and MeCN-HK samples were soaked in pure DCM at room temperature for 5 min, repeated five times to ensure complete exchange. Subsequent ^1H NMR spectroscopy after digesting each sample in deuterated sulfuric acid (D_2SO_4) revealed the disappearance of precoordinating solvent peaks corresponding to EtOH, MeOH, and MeCN (Fig. 4a and b). The loss of these characteristic resonances indicates their dissociation from Cu(II) *via* coordination exchange with DCM. Remarkably, this process
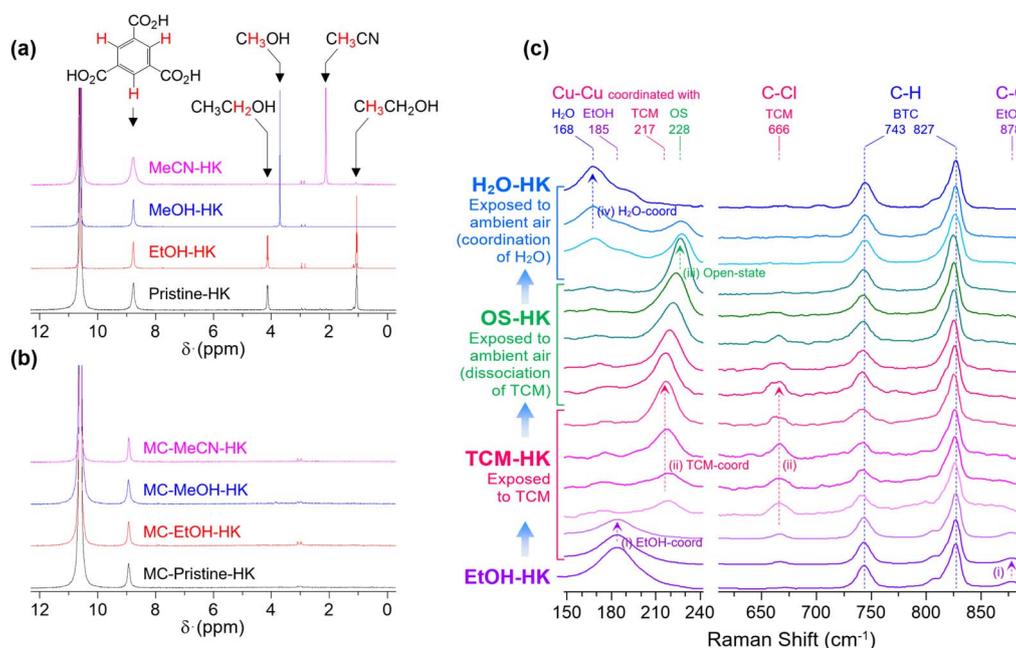

Fig. 4 (a and b) ^1H NMR spectra of pristine-, EtOH-, MeOH-, and MeCN-coordinated HKUST-1 (a) before and (b) after DCM treatment (MC-indicates post-DCM). Spectra were collected after complete digestion of the powders in D_2SO_4. Reproduced with permission from ref. 33, Copyright 2015, American Chemical Society. (c) *In situ* Raman spectra of DMF-coordinated HKUST-1 showing sequential changes upon exposure to EtOH, then DCM, and finally ambient air, evidencing stepwise coordination exchange and regeneration of the open-metal state. Reproduced with permission from ref. 35, Copyright 2018, American Chemical Society.
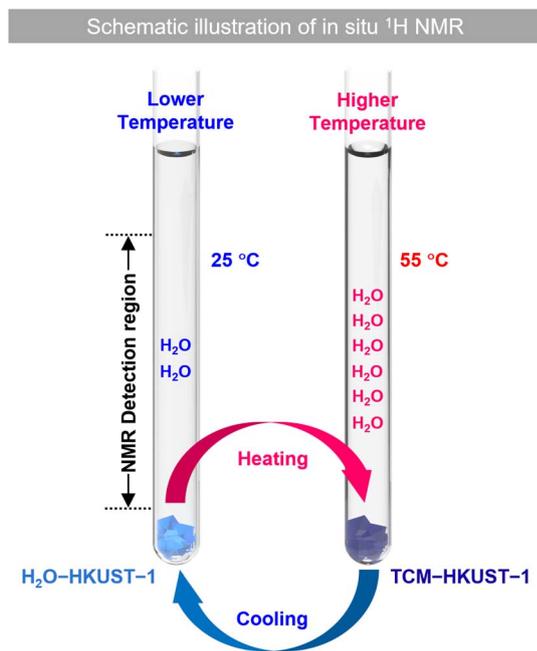
This journal is © The Royal Society of Chemistry 2026

J. Mater. Chem. A, 2026, **14**, 9088–9114 | **9091**

Fig. 6 Schematic illustration of the *in situ* ^{1}H NMR setup for probing temperature-dependent coordinative equilibrium: HKUST-1 crystals are immersed in TCM-d containing a defined amount of H_2O, and spectra are recorded at 25 °C and 55 °C during heating/cooling cycles to quantify the fractions of coordinated *vs.* free H_2O within the NMR detection region. Reproduced with permission from ref. 32, Copyright 2022, Royal Society of Chemistry.

proceeded entirely at room temperature, highlighting the inherent dynamicity of coordination bonding at OMSs.

Later, TCM was also shown to exhibit similar exchange behavior.[35] ^{1}H NMR spectra of TCM-treated HKUST-1 displayed the complete removal of precoordinated solvents (*i.e.*, MeOH, EtOH, and MeCN), analogous to the DCM-treated samples. *In situ* Raman spectroscopy corroborated these results: during TCM treatment of EtOH-HK, the Cu–Cu stretching vibrational band shifted initially from 185 cm^{-1} to 217 cm^{-1} upon exposure to TCM, consistent with the formation of a weaker TCM coordination bond (Fig. 4c). Upon air exposure, the band further shifted to ~228 cm^{-1}, reflecting TCM dissociation and regeneration of the coordination-free open-metal state. These findings confirm that, in a confined environment, even intrinsically weak donors, such as DCM and TCM, can mediate coordination exchange through reversible association-dissociation dynamics.

2.1.3 Dynamic coordinative equilibrium at different temperatures. Thermal energy provides a sensitive probe of coordination dynamics at OMSs. In a static system, coordination strength would remain less affected by temperature variance. However, in a dynamic equilibrium system, thermal energy perturbs the balance between associated and dissociated states, facilitating transient bond cleavage and reformation. Hence, examining temperature-dependent coordination exchange behavior elucidates the thermally activatable nature of dynamic bonding.

The temperature dependence of coordination exchange was first examined using ^{1}H NMR spectroscopy, which tracked the

replacement of precoordinated MeOH in HKUST-1 after TCM treatment (Fig. 5).[35] Specifically, MeOH-HK crystals were soaked in pure TCM for 5 min at 25 °C and 55 °C, respectively, and the procedure was repeated until the MeOH-coordination disappeared completely. As a result, nine repetitions were required at 25 °C to achieve complete exchange, whereas only four were needed at 55 °C, clearly demonstrating the thermal acceleration of the bond dissociation. The enhancement arises because elevated temperature (i) promotes the dissociation of strong coordination bonds and (ii) increases translational and rotational motions of unbound TCM molecules, thereby amplifying collision frequency within the nanopores.

To probe this effect more directly, *in situ* ^{1}H NMR experiments were designed to monitor association and dissociation events within the pores.[32] Fully desolvated "activated" HKUST-1 (Act-HK) crystals were introduced into deuterated TCM (TCM-d) solvent containing a 1 : 1 stoichiometric ratio of H_2O to Cu(II) sites (Fig. 6). Upon immersion, the integral of the H_2O signal in the solvent decreased to 25%, indicating that 75% of H_2O molecules coordinated to Cu(II) centers in HKUST-1 crystals (Fig. 7). The remaining 25% unbound H_2O molecules signified an equilibrium between coordinated and free states. Increasing the temperature, however, shifted this balance: at 40 °C, the unbound fraction inreased to 75%, and at 55 °C, to 93%, revealing substantial dissociation. Cooling back to 40 °C and 25 °C restored the initial integral values (75% and 26%, respectively), confirming reversibility. Similar temperature-dependent trends were observed for MeOH and EtOH, while DMF—owing to its stronger coordination—exhibited only a minor change (~14%). These findings demonstrate a temperature-dependent "dynamic coordinative equilibrium" between associated and dissociated states around OMSs.

2.1.4 Multiple coordination exchange. While weakly coordinating solvents such as DCM and TCM have been shown to effectively replace moderately coordinating molecules (*e.g.*, MeOH, EtOH, MeCN, and PhOH), their ability to displace more strongly coordinating molecules remains inherently limited. For instance, DMF, *N,N*-diethylformamide (DEF), and dimethyl sulfoxide (DMSO)—well-known for their strong coordination to Cu(II) paddlewheel nodes—cannot be completely exchanged by DCM or TCM under ambient conditions, even after several tens of treatments. To overcome this limitation, the concept of "multiple coordination exchange" was introduced (Fig. 8a).[34] In this stepwise approach, the strongly coordinating molecules initially bound to the Cu(II) nodes of HKUST-1 are first replaced by moderately coordinating ones (*i.e.*, MeOH, EtOH, and MeCN), which are then subsequently exchanged by weakly coordinating molecules (*i.e.*, TCM and DCM). This multistep process leverages the transient dissociation and reassociation dynamics inherent in the coordination bonds at OMSs.

For instance, ^{1}H NMR spectroscopy provided clear evidence of this process. Upon four consecutive MeCN treatments, the NMR peak of DMF completely disappeared, indicating full substitution. Five subsequent cycles of DCM treatment removed MeCN coordination entirely (Fig. 8b). Similar sequential exchanges were observed for MeOH and EtOH—three cycles of MeOH or nine of EtOH replaced DMF, followed by DCM treatments (nine for
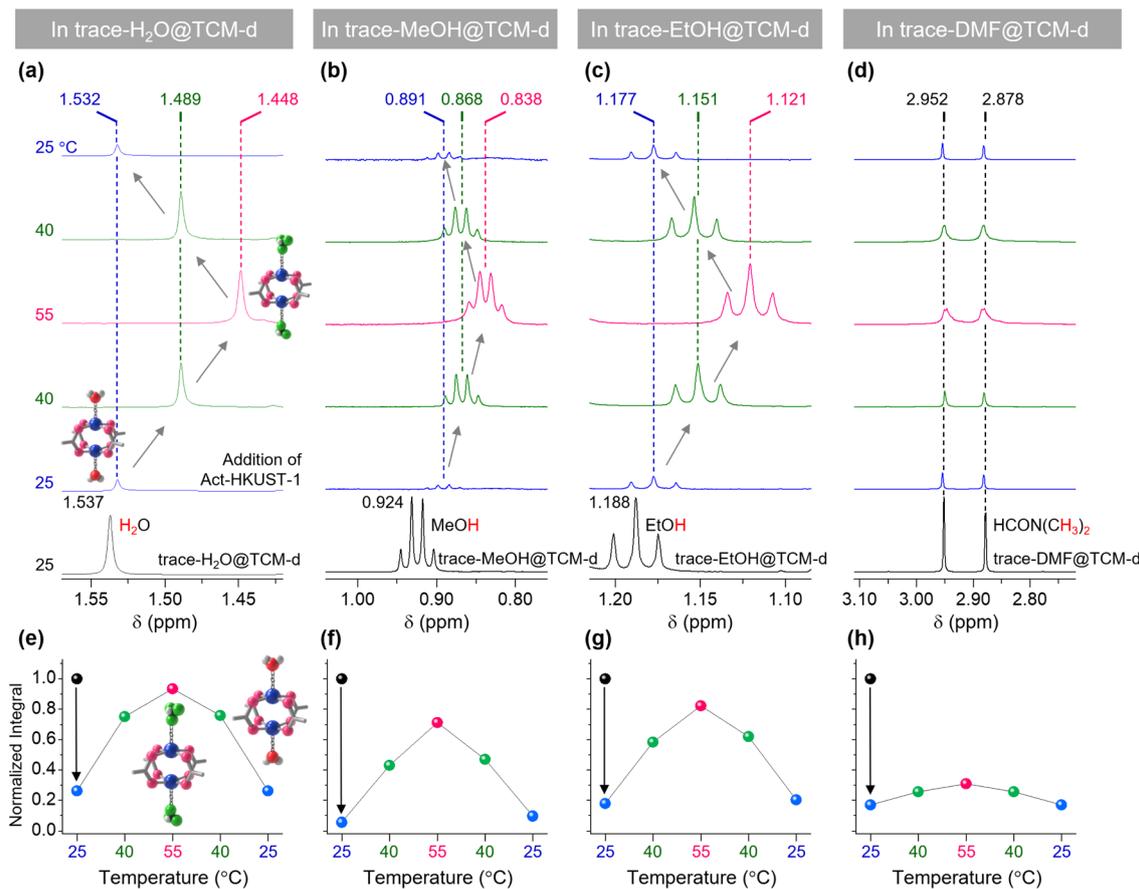
9092 | *J. Mater. Chem. A*, 2026, **14**, 9088–9114

This journal is © The Royal Society of Chemistry 2026

Fig. 7 (a–d) *In situ* ^{1}H NMR spectra and (e–h) corresponding integrated peak area profiles for (a and e) H$_2$O in H$_2$O@TCM-d, (b and f) MeOH in MeOH@TCM-d, (c and g) EtOH in EtOH@TCM-d, and (d and h) DMF in DMF@TCM-d, measured with small Act-HK crystals (*ca.* 10 μm) at 25 °C (blue), 40 °C (green), and 55 °C (red) during heating and cooling. Spectra of (a) H$_2$O@TCM-d, (b) MeOH@TCM-d, (c) EtOH@TCM-d, and (d) DMF@TCM-d without Act-HK crystals (black) are shown for comparison. Peak positions/integrals were taken from the hydroxyl protons (H$_2$O, MeOH, and EtOH) or methyl protons (DMF); integrals were normalized using residual CHCl$_3$ in CDCl$_3$. Reproduced with permission from ref. 30. Copyright 2022, Royal Society of Chemistry. Reproduced with permission from ref. 32, Copyright 2022, Royal Society of Chemistry.

MeOH; five for EtOH) that eliminated the intermediates. These observations establish multiple coordination exchange as a general, stepwise route to achieve complete substitution, thereby providing a method to activate MOFs at room temperature.

To provide direct evidence for this process, *in situ* ^{1}H NMR experiments were performed. Specifically, DMF-HK crystals were immersed in deuterated acetonitrile (CD$_3$CN), and the amount of DMF released into the solvent—corresponding to dissociation from the Cu(II) centers during dynamic coordination exchange—was monitored over time (Fig. 9a). Initially, no DMF resonance was observed in the CD$_3$CN solvent; however, the DMF signal gradually increased and reached a plateau after 25 minutes, indicating that the exchange from DMF to CD$_3$CN had reached completion (Fig. 9b and c). To quantify the remaining solvent molecules further, the exchanged crystals were digested in D$_2$SO$_4$, revealing that only ~1.8% of DMF remained within the framework (Fig. 9c). A similar trend was observed in the reciprocal process, where MeCN-HK crystals treated with CD$_2$Cl$_2$ exhibited a plateau after 15 minutes with ~4.0% residual MeCN (Fig. 9d and e). These findings collectively confirm that coordination exchange occurs dynamically through reversible dissociation–association equilibria at the Cu(II) nodes.

To complement the NMR analyses, *in situ* Raman spectroscopy was employed to monitor sequential changes in the Cu–Cu stretching vibration as the coordination environment evolved. The Cu–Cu band exhibited a progressive blue-shift from 175 cm^{-1} for DMF-HK to 185 cm^{-1} after EtOH exchange, and finally to 213 cm^{-1} following DCM replacement. This systematic shift reflects a gradual weakening of coordination strength as strongly coordinating molecules are stepwise substituted by weaker ones. Taken together, these results demonstrate that multiple coordination exchange provides an effective route for achieving complete solvent substitution at OMSs through reversible and competitive coordination equilibria. This mechanism not only reinforces the dynamic nature of coordination bonding in MOFs but also highlights the intricate balance between thermodynamics and kinetics that governs ligand exchange in confined environments.

2.2 Laser-induced dynamicity of the metal–guest molecule bond

Beyond supplying a thermal energy stimulus (see above), light irradiation provides an additional external stimulus to probe dynamic bonding in MOFs. In 2020, Jeong and colleagues
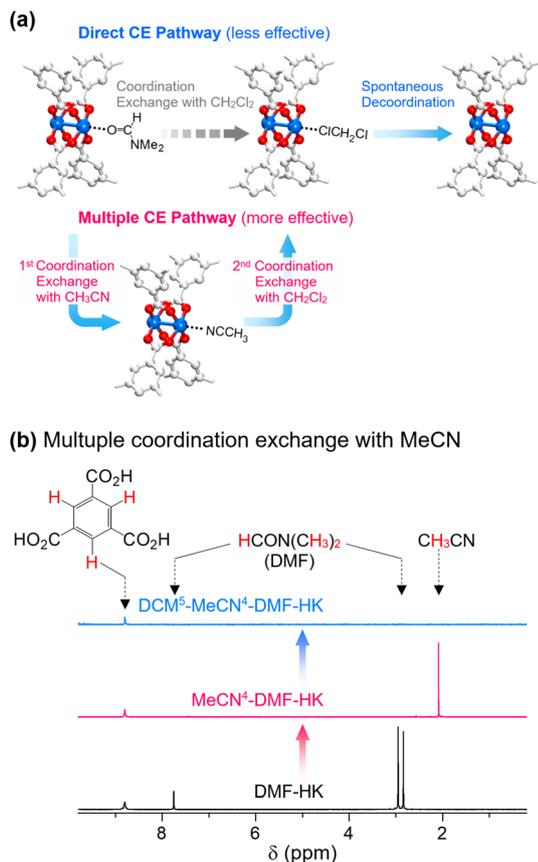
This journal is © The Royal Society of Chemistry 2026

J. Mater. Chem. A, 2026, **14**, 9088–9114 | **9093**

Fig. 8 (a) Schematic illustration of direct *versus* multiple coordination exchanges for chemical activation of the Cu(II) paddlewheel node in HKUST-1; H atoms on benzene carbons are omitted for clarity. (b) ^{1}H NMR spectra of DMF-coordinated HKUST-1 before treatment, after initial MeCN exchange, and after subsequent DCM exchange; superscripts denote the number of treatment repetitions. Spectra were acquired after complete digestion of the powders in D_2SO_4. Reproduced with permission from ref. 34, Copyright 2017, American Chemical Society.

demonstrated that visible laser irradiation could induce dissociation of guest molecules coordinated to Cu(II) paddlewheel nodes in HKUST-1.[38] Notably, this dissociation occurs not through direct photolysis but *via* nonradiative thermal relaxation at Cu(II) centers (Fig. 10a). Upon visible light absorption, Cu–Cu nodes undergo d–d transitions from the ground-state t_{2g} to excited-state e_g orbitals. Electrons in the excited state (E) relax to a spillover state (S) through a vibrational transition (E → S) at room temperature, and then return to the ground state (G) nonradiatively, releasing localized heat energy. Continuous excitation sustains this cycle, gradually accumulating sufficient heat energy within nanopores to surpass the coordination bond dissociation threshold (Fig. 10b).

This process was evidenced by *in situ* Raman spectroscopy. Upon 532 nm laser irradiation (1.5–8.0 mW, 5 min), the Cu–Cu vibrational bands of H_2O-HK, MeOH-HK, EtOH-HK, and DMF-HK shifted toward ~230 cm^{-1}, corresponding to the open-metal state (Fig. 11). A distinct threshold laser power—the critical power—was observed for each solvent: MeOH (1.5 mW)

< EtOH (2.0 mW) < H_2O (3.3 mW) < DMF (8.0 mW), consistent with their relative coordination strengths [MeOH ≈ EtOH < H_2O < DMF] and boiling points [MeOH (64 °C) < EtOH (78 °C) < H_2O (100 °C) < DMF (153 °C)]. These findings establish that even strongly coordinated guest molecules at OMSs are not static but can be reversibly dissociated under light-induced localized heating. Crucially, this process is fully reversible—the coordination bonds reform once the excitation ceases—demonstrating a light-responsive dynamic equilibrium at OMSs. Nonradiative relaxation thus represents a powerful, stimulus-responsive mechanism for probing the dynamic nature of the coordination bond in MOFs.

3 Dynamicity of metal–linker coordination bonding

Metal–linker dynamic bonding refers to the reversible and transient dissociation–association of coordination bonds between metal nodes and organic linkers within a framework. Unlike the dynamic bonding at OMSs that involves guest molecules, metal–linker dynamics occur intrinsically within the backbone of the framework. Although these bonds have traditionally been regarded as rigid linkages that maintain structural integrity, growing evidence indicates that they are not permanently static but can respond dynamically to external stimuli while preserving overall crystallinity.

This section highlights spectroscopic evidence showing that external perturbations can modulate the equilibrium between the associated and dissociated states of metal–linker bonds. (3.1) Heating serves as a typical stimulus by providing thermal energy that enhances bond vibrations and shifts the equilibrium toward transient dissociation. (3.2) Light irradiation can also induce reversible, partial dissociation of metal–linker bonds *via* ligand-to-metal charge transfer (LMCT), temporarily converting bidentate coordination to monodentate before returning to the ground state. (3.3) Guest molecules influence this equilibrium by stabilizing partially dissociated configurations, (3.4) while reducing crystal size enhances bond flexibility through surface effects. Collectively, these pathways demonstrate how metal–linker dynamic bonding governs the responsiveness of MOFs to external stimuli, offering new avenues for designing functionally adaptive frameworks.

3.1 Temperature-dependent dynamicity of the metal–linker bond

Temperature variance provides a powerful probe for dynamic bonding, as thermal energy drives reversible association and dissociation of coordination bonds. In a dynamic system, increasing temperature promotes transient bond cleavage, and corresponding vibrational shifts can reveal that bonds exist in equilibrium rather than a static state.[62,63] In carboxylate-based MOFs, these dynamics can be tracked through vibrational spectroscopy by monitoring the C–O stretching band, which is electronically coupled to the metal–oxygen bond (Fig. 12a). From a molecular orbital perspective, the C–O bond consists of σ and π bonding orbitals, π* antibonding orbitals, and oxygen-
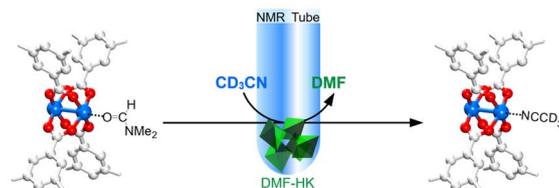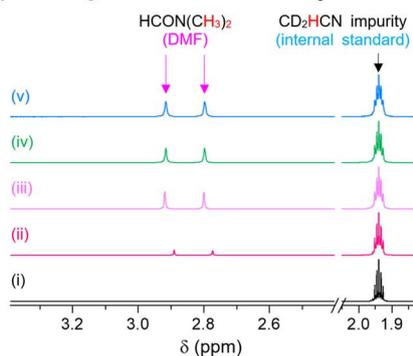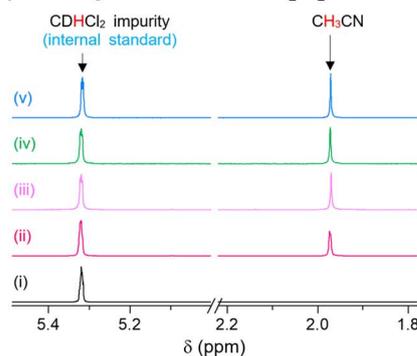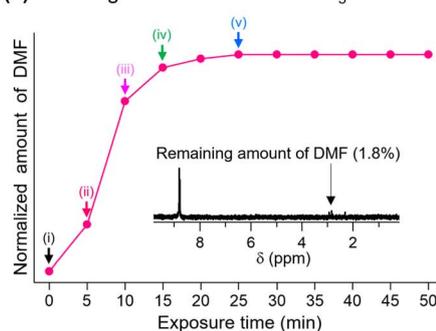
9094 | *J. Mater. Chem. A*, 2026, **14**, 9088–9114

This journal is © The Royal Society of Chemistry 2026
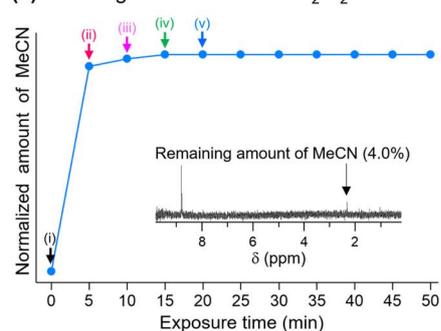
Fig. 9 (a) Schematic illustration of the *in situ* ^{1}H NMR experiment for directly monitoring coordination exchange: precoordinated DMF in HKUST–1 is substituted by MeCN-d$_3$ (CD$_3$CN), and the amount of DMF released into the solvent is quantified; H atoms on benzene carbons are omitted for clarity. (b) *In situ* time-course ^{1}H NMR spectra of MeCN-d$_3$ containing DMF-HK crystals, using the CD$_2$HCN impurity as an internal standard. (c) Normalized amount of dissolved DMF *versus* exposure time; inset shows the *ex situ* ^{1}H NMR spectrum of the reacted crystals after dissolution in D$_2$SO$_4$ (residual DMF). (d) *In situ* time-course ^{1}H NMR spectra of CD$_2$Cl$_2$ containing MeCN-HK crystals, using the CDHCl$_2$ impurity as an internal standard. (e) Normalized amount of dissolved MeCN *versus* exposure time; inset shows the *ex situ* spectrum of the reacted crystals after dissolution in D$_2$SO$_4$ (residual MeCN). Reproduced with permission from ref. 34, Copyright 2017, American Chemical Society.

localized nonbonding orbitals (Fig. 12b). Strong M–O coordination withdraws electrons partially from the nonbonding and antibonding orbitals, increasing the C–O bond order and shifting the vibrational frequency to higher energy. Conversely, weaker coordination results in a greater electron density on oxygen, which lowers the bond order and produces a red shift. Thus, temperature-dependent shifts of the carboxylate stretching vibrational bands provide direct spectroscopic evidence for metal–linker dynamics.

Brozek and coworkers demonstrated temperature-dependent metal–linker dynamics in carboxylate-based MOFs using variable-temperature diffuse reflectance infrared Fourier transform spectroscopy (VT-DRIFTS).[64] Representative frameworks including HKUST-1, UiO-66, MIL-125, MIL-125-NH$_2$, MOF-5, MUV-10(Ca), MUV-10(Mn), Zn-MOF-74, and Mg-MOF-74 were analyzed from −100 to 200 °C. As the temperature increased, the

symmetric and asymmetric COO$^-$ vibrational bands exhibited red shifts, indicating the existence of a dynamic equilibrium between associated and dissociated coordination states. Each spectrum could be deconvoluted into two components corresponding to these states (Fig. 12c). The ratio of their relative intensities yielded a flexibility constant {ln(K_{flex}), where K_{flex} = [dissociation]/[association]}.[22] For HKUST-1 at room temperature, ln(K_{flex}) ≈ 0.3—comparable to molecular metal–carboxylate complexes—confirming significant metal–linker flexibility. In contrast, more robust frameworks such as UiO-66 and MIL-125 displayed a smaller red shift, reflecting stronger coordination and suppressed temperature-induced dynamics.

Spin-crossover (SCO) frameworks further exemplify temperature-driven dynamic bonding, as their spin transitions directly modulate metal–linker bond lengths and strengths.[65] In the low-spin state, bonds are shorter and stronger, while in the
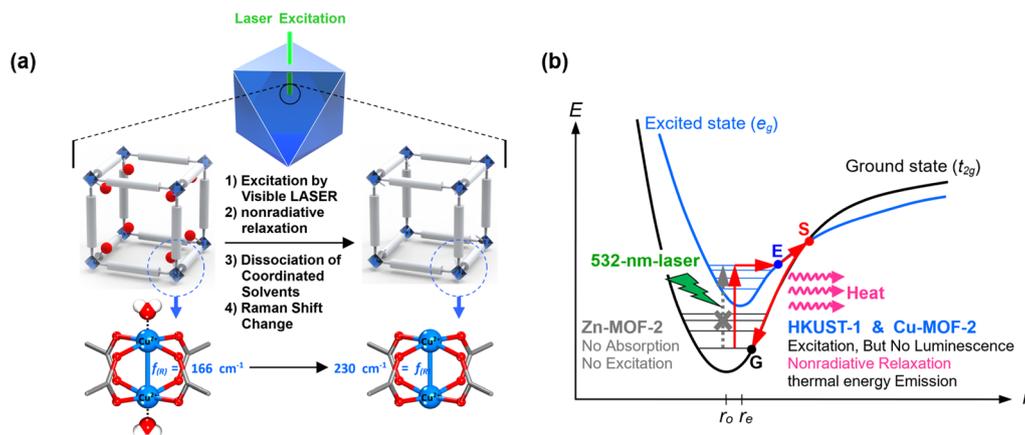
This journal is © The Royal Society of Chemistry 2026

J. Mater. Chem. A, 2026, **14**, 9088–9114 | **9095**

Fig. 10 (a) Laser-induced dissociation of H_2O coordinated at Cu(II) paddlewheel nodes *via* nonradiative thermal relaxation, accompanied by a blue shift of the Cu–Cu Raman band from ~166 to ~230 cm^{-1}. (b) Configurational coordinate diagram proposing the nonradiative relaxation pathway in Cu(II)-based MOFs under 532 nm excitation (in contrast with Zn-MOF-2, which lacks absorption/excitation). Reproduced with permission from ref. 38, Copyright 2020, American Chemical Society.

high-spin state, they elongate and weaken. These reversible structural changes provide direct evidence of dynamic metal–linker bonding (Fig. 13a). An Fe-based MOF, Fe(1,2,3-triazolate)$_2$ [Fe(TA)$_2$], serves as a representative SCO system. The triazolate vibrational band near 1230 cm^{-1}, monitored by VT-DRIFTS, red-shifted to lower wavenumbers at temperatures

below the transition temperature as the Fe–N bonds gradually weakened. Above the transition temperature, however, the band blue-shifted due to the rearrangement of Fe–N vibrational modes upon its entering the high-spin state (Fig. 13b). Iso-structural analogues M(TA)$_2$ (M = Mn, Co, Zn, Cu) lacking SCO behavior exhibited different trends: Mn, Co, and Zn frameworks
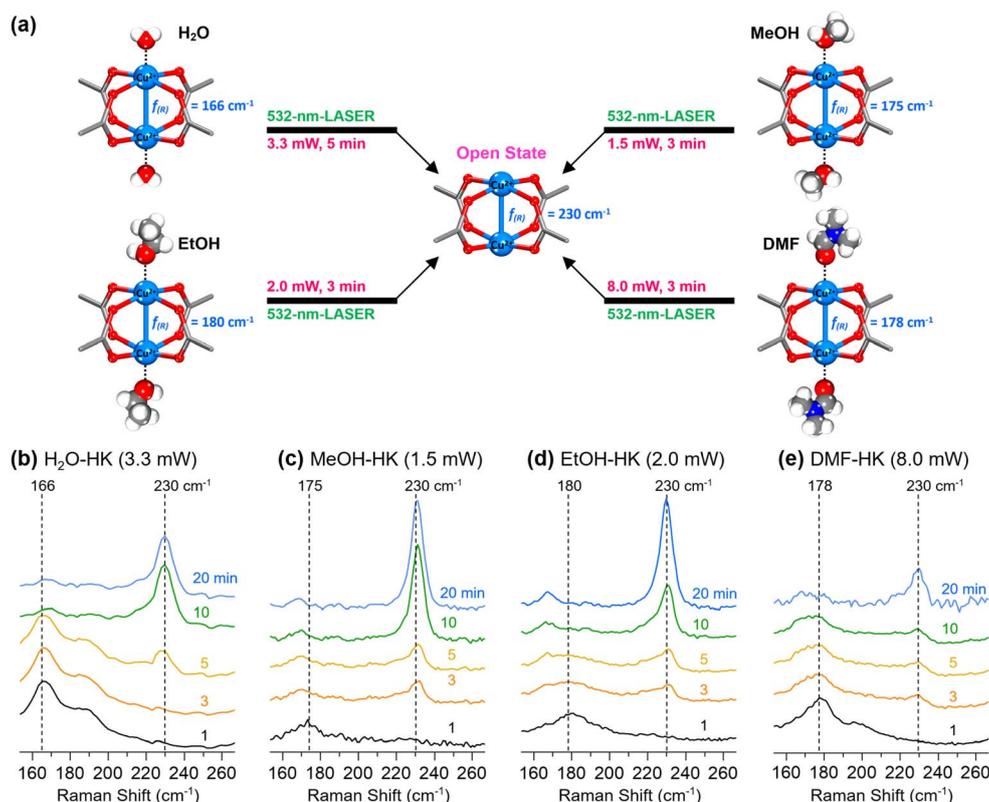
Fig. 11 (a) Schematic illustrations of H_2O-, MeOH-, EtOH-, and DMF-coordinated Cu(II) paddlewheel nodes in HKUST-1 and their conversion to the open state under 532 nm laser irradiation *via* nonradiative relaxation, with corresponding shifts of the Cu–Cu Raman band toward ~230 cm^{-1}. Successive *in situ* Raman spectra of (b) H_2O-HK at 3.3 mW, (c) MeOH-HK at 1.5 mW, (d) EtOH-HK at 2.0 mW, and (e) DMF-HK at 8.0 mW, showing time-dependent blue shifts consistent with solvent dissociation. Reproduced with permission from ref. 38, Copyright 2020, American Chemical Society.

9096 | *J. Mater. Chem. A*, 2026, **14**, 9088–9114

This journal is © The Royal Society of Chemistry 2026

Fig. 12 (a) Illustration of carboxylate vibrations (highlighted in blue) that can be monitored by VT-DRIFTS as proxies for metal–oxygen interactions because they act as coupled oscillators. Reproduced with permission from ref. 22, Copyright 2024, American Chemical So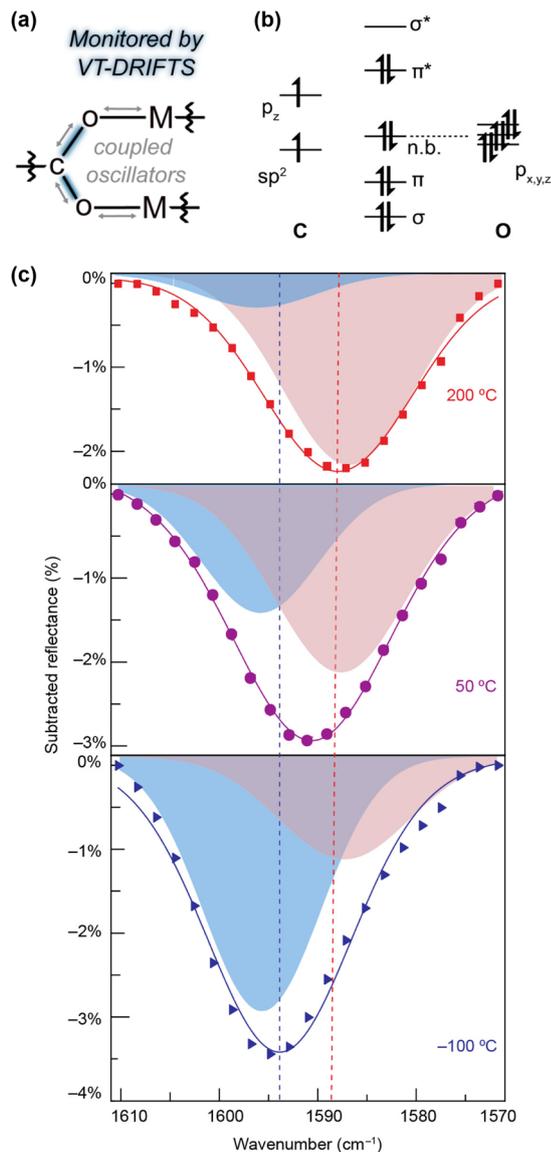ciety. (b) Molecular-orbital diagram of the carbonyl in a carboxylate group. (c) Global curve fits of HKUST-1 asymmetric carboxylate stretches at −100, 50, and 200 °C, deconvoluted into two components with fixed peak positions at 1596 cm^{-1} (blue) and 1587 cm^{-1} (red) and variable areas; markers are experimental data and solid lines are Gaussian fits. Reproduced with permission from ref. 64, Copyright 2020, American Chemical Society.

showed linear red shifts with a temperature increase, consistent with thermally activated dynamic bonding, whereas Cu(TA)$_2$ displayed a nonlinear shift, reflecting its crystalline phase transition from tetragonal to cubic. These results demonstrate that dynamic bonding operates not only in spin-transition systems but also in thermal-responsive frameworks.

Overall, these studies show that thermal energy (or temperature variance) modulates the equilibrium between associated and dissociated coordination states, offering direct spectroscopic

evidence of metal–linker dynamics. Such temperature-dependent behaviors manifest in diverse forms—from electronic spin transitions to structural phase changes—highlighting the fundamental role of dynamic bonding in MOF chemistry.

3.2 Photoinduced dynamicity of the metal–linker bond

Photoexcitation provides another route to induce metal–linker dynamics by transiently weakening coordination bonds. Using MIL-101(Fe), Morris and coworkers demonstrated that visible-light excitation leads to reversible, partial dissociation of the carboxylate linker from the Fe–oxo node, as revealed by visible transient absorption and time-resolved infrared spectroscopies, as well as computational studies (Fig. 14a).[66] Time-resolved infrared spectra showed a decrease in the bands associated with the bidentate coordination mode and the emergence of new features corresponding to monodentate binding. Specifically, ground-state bleaches were observed at 1400 and 1590 cm^{-1} (symmetric and asymmetric COO$^-$ stretching vibrations of bidentate carboxylates, respectively), accompanied by new absorptions at 1360 and 1480 cm^{-1} indicative of monodentate coordination. Additional transient signals at 1710 cm^{-1} (C=O stretching) and 1190 cm^{-1} (C–O single-bond character) confirmed the presence of the monodentate intermediate (Fig. 14b). Collectively, these changes signify a reversible, photoinduced transition from bidentate bridging in the ground state to a monodentate configuration in the excited state rather than irreversible bond cleavage.

Kinetic analysis of the time-resolved infrared data revealed monoexponential decays with an average lifetime of 28.2 µs,
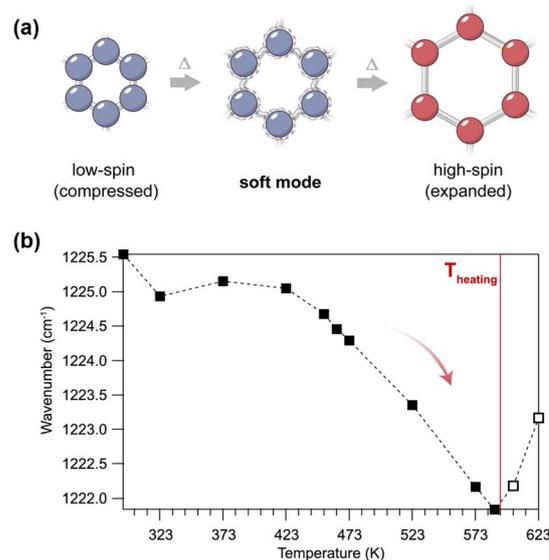
Fig. 13 (a) Schematic of the thermally driven spin-crossover in Fe(1,2,3-triazolate)$_2$, showing lattice expansion from the low-spin (compressed) to the high-spin (expanded) state with an accompanying soft-mode coupling; the six-membered ring highlights the pore aperture. Reproduced with permission from ref. 22, Copyright 2024, American Chemical Society. (b) Temperature-dependent shift of vibrational mode "X" during heating, illustrating the approach to the spin-transition regime. Reproduced with permission from ref. 65, Copyright 2021, American Chemical Society.

This journal is © The Royal Society of Chemistry 2026

J. Mater. Chem. A, 2026, 14, 9088–9114 | 9097

which closely agrees with the LMCT lifetimes determined from visible transient absorption measurements. This agreement confirms that the structural perturbation at the Fe–carboxylate bond is directly coupled to the LMCT state. Computational results further corroborated this mechanism, showing that excitation promotes electron density from a bonding Fe–carboxylate orbital to an Fe-centered antibonding orbital, transiently weakening the Fe–O coordination bonding (Fig. 14a). These findings establish that the Fe–carboxylate bond can reversibly dissociate on a microsecond timescale before re-forming, exemplifying the ultrafast dynamicity of metal–linker coordination.

3.3 Guest-molecule-triggered dynamicity of the metal–linker bond

Guest molecules can also modulate metal–linker dynamics by shifting the equilibrium between associated and dissociated states.[67] In UiO-66, VT-DRIFTS spectra reveal enhanced dynamicity in the presence of guest molecules compared to that under

Fig. 14 (a) Schematic of the photoinduced process in MIL-101(Fe): excitation at 428 nm promotes an electron from a bonding Fe-BDC orbital to a Fe(III)-centered antibonding orbital, transiently weakening Fe–carboxylate coordination (representative orbitals shown). (b) Time-resolved infrared absorption difference spectra of MIL-101(Fe) at selected delay times after photoexcitation. Reproduced with permission from ref. 66, Copyright 2024, American Chemical Society.

vacuum conditions. Under dynamic vacuum, UiO-66 exhibits a temperature-dependent red shift of the asymmetric COO^- vibrational band with a slope of approximately -0.015 cm^{-1} K^{-1} (Fig. 15a). After water-included air exposure, the slope increases to -0.051 cm^{-1} K^{-1}—the steepest value reported for MOFs (Fig. 15b). This enhancement is attributed to interactions between Lewis-basic H_2O molecules and Zr–O carboxylate bonds, which weaken the coordination and, thereby, shift the equilibrium toward partially dissociated states.

Further experiments confirmed that this effect extends to other solvent environments. At 298 K, triethyl amine (Et_3N), EtOH, DMF, and THF all induced additional red shifts of the COO^- vibrational bands relative to activated UiO-66 (Fig. 15c–e). The extent of these shifts correlates systematically with the Gutmann donor number of the solvent. Et_3N, possessing the highest donor number (61), produced the largest red shift and a flexibility constant of $\ln(K_{\text{flex}}) = -0.61$, indicating dominance of the dissociated state at room temperature.

These results demonstrate that guest molecules promote dissociation by interacting with metal–linker bonds and stabilizing partially uncoordinated configurations. The guest-dependent red-shift slopes and flexibility constants quantitatively capture this enhanced dynamicity. Such guest-induced flexibility provides a mechanistic foundation for dynamic processes that require temporary access to coordinatively saturated metal sites, including post-synthetic modification, gas adsorption, and catalysis.

3.4 Crystal-size-dependent dynamicity of the metal–linker bond

The crystal size of an MOF has a critical influence on metal–linker dynamics. Brozek and coworkers systematically investigated this dependence by comparing MIL-125, UiO-66, and ZIF-8 nanocrystals with varying dimensions.[68] For MIL-125, 79 nm crystalline particles exhibited an optical gap of ~3.82 eV at low temperature, which decreased by ~600 meV upon heating. Larger particles (215 nm and 424 nm) displayed markedly smaller changes. UiO-66 followed the same trend, with smaller crystals showing stronger temperature-induced gap narrowing, whereas ZIF-8 showed negligible variation, consistent with its rigid metal–imidazolate framework.

The pronounced size dependence of optical gap shifts provides clear evidence for dynamic bonding. Smaller particles exhibit greater temperature-dependent changes because their metal–linker bonds can more easily access transiently dissociated configurations. This behavior reflects an increased surface-to-core ratio in terms of the number of atoms, where surface sites experience reduced stabilization, leading to weaker and more flexible coordination bonds. Consequently, decreasing crystal size enhances overall lattice flexibility and amplifies dynamic bonding behavior.

4 Application of the metal−guest molecule dynamic bonding

The concept of dynamic bonding of guest molecules at OMSs provides a unifying design principle for diverse MOF
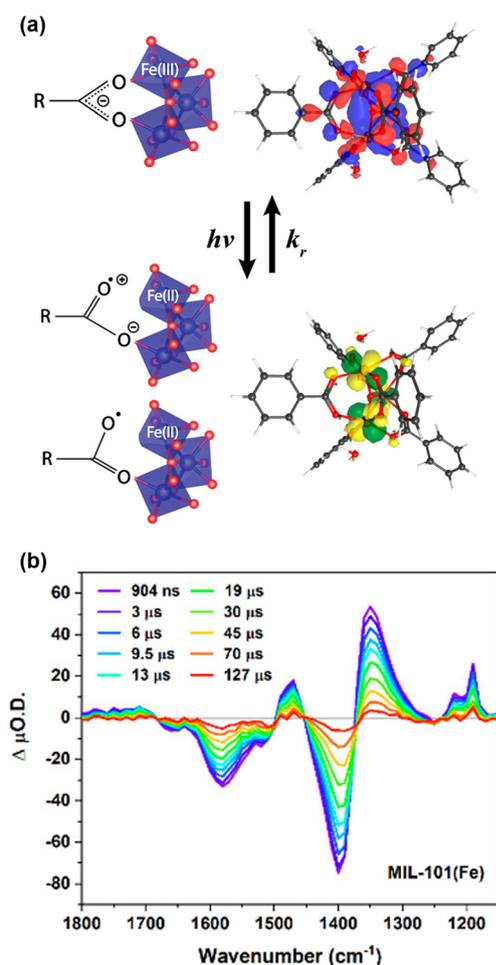
9098 | *J. Mater. Chem. A*, 2026, **14**, 9088–9114

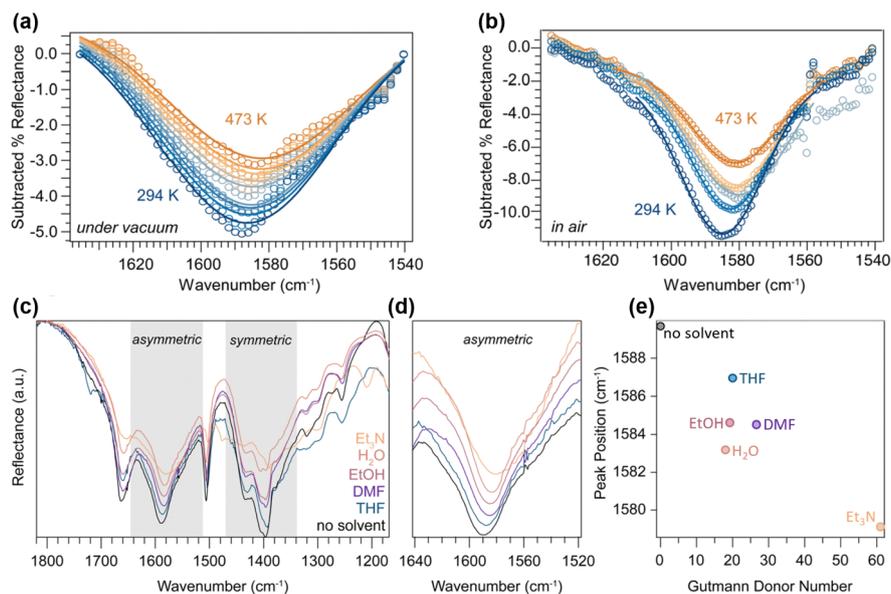This journal is © The Royal Society of Chemistry 2026

Fig. 15 (a) Subtracted-reflectance VT-DRIFTS of the UiO-66 asymmetric carboxylate stretching vibration under dynamic vacuum at 294–473 K. (b) Corresponding spectra collected in air at 294–473 K, showing enhanced red shifts relative to vacuum. (c) Solvent-dependent VT-DRIFTS of UiO-66 highlighting asymmetric and symmetric carboxylate stretching vibrations. (d) Enlarged view of the asymmetric stretching vibration, demonstrating solvent-specific red shifts. (e) Correlation of asymmetric-stretching band position with the Gutmann donor number. Reproduced with permission from ref. 67, Copyright 2023, Royal Society of Chemistry.

applications. (4.1) In activation, reversible coordination exchange enables the removal of strongly coordinating solvent molecules without requiring harsh thermal treatment, as demonstrated by the chemical activation performed with weakly coordinating DCM or TCM, and in gas-flow activation using inert gases such as nitrogen and argon. (4.2) In catalysis, the dynamic association–dissociation of guest molecules directly modulates the accessibility of the catalytic substance to OMSs; weakly coordinating environments maintain active centers in an open state, thereby enhancing reactivity. (4.3) In gas adsorption, the dynamic bonding at OMSs underpins the cooperative uptake of acidic gases such as CO_2 and CS_2 in amine-grafted MOFs, leading to high capacities.

4.1 Non-thermal methods for activation *via* dynamic metal–guest molecule bonding

Activation—a process that removes both pore-filling species and strongly coordinating molecules from metal nodes—is a prerequisite step for exploiting the intrinsic porosity and open-metal state of MOFs.[36,69,70] In particular, dissociation of coordinated solvents at OMSs is essential because these sites function as active centers in adsorption, separation, and catalysis.

Thermal activation, which removes both pore-filling and coordinating molecules by heating under vacuum,[71–73] has been the most widely used method, whereas most alternative methods primarily purge pore-filling solvent.[74,75] Thermal activation, nevertheless, has inherent limitations: strongly coordinating solvents such as DMF, DEF, or DMSO require high temperatures that can trigger structural collapse or undesired phase transitions. These challenges are particularly acute for

thermally fragile MOFs and composites, where high-temperature treatment can damage the crystallinity or polymer matrices. Thus, such constraints motivate non-thermal strategies.

To address this challenge, the Jeong group introduced chemical activation and gas-flow activation methods, both of which leverage metal–guest dynamic bonding without the need for external heat energy. In chemical activation, weakly coordinating molecules (DCM and TCM) exchange precoordinated solvent molecules at OMSs and then dissociate spontaneously, delivering complete activation under mild conditions while preserving framework integrity (Fig. 16a). More recently, gas-flow activation using inert gases (N_2 and Ar) removed coordinated solvents *via* dynamic dissociation–association: continuous gas flow supplies collision energy that escorts transiently dissociated molecules out of the pores, lowering activation temperatures relative to the static thermal activation method. Collectively, these strategies activate MOFs under non-destructive, low-energy conditions by exploiting dynamic coordination at OMSs, thereby expanding accessible pore space and enabling the operationality of OMSs under mild conditions.

4.1.1 Chemical activation. Weakly coordinating DCM and TCM offer a purely chemical route for activating MOFs under ambient conditions by harnessing the intrinsic dynamicity of metal–guest bonding. Through transient coordination followed by spontaneous dissociation, these molecules remove strongly coordinating solvents at OMSs without the structural damage often caused by thermal activation. The first demonstration employed DCM.[33] Systematic studies on HKUST-1 and Cu-MOF-2 showed that the repeated room-temperature soaking of a MOF in DCM effectively removed precoordinated H_2O, EtOH, MeOH,

This journal is © The Royal Society of Chemistry 2026

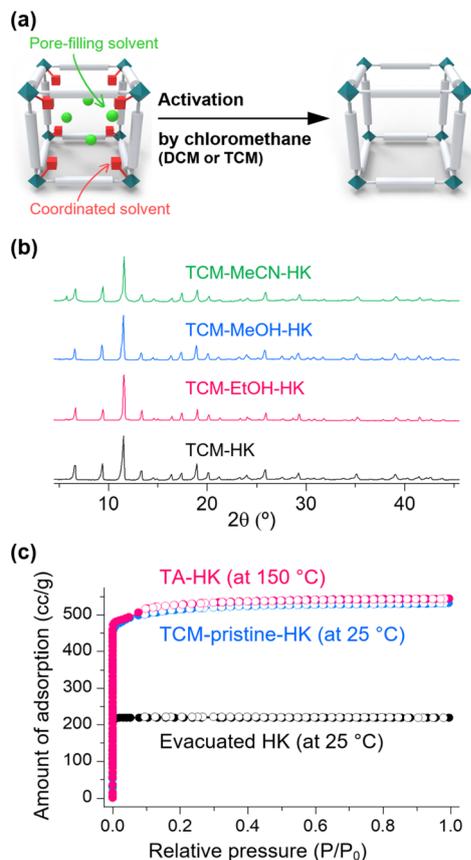*J. Mater. Chem. A*, 2026, **14**, 9088–9114 | **9099**

Fig. 16 (a) Schematic illustrations of an MOF unit cell before and after removal of coordinated and pore-filling solvents by chloromethane (DCM or TCM) treatment. Reproduced with permission from ref. 36, Copyright 2018, Royal Society of Chemistry. (b) Powder X-ray diffraction patterns of TCM-treated HKUST-1 starting from EtOH-, MeOH-, and MeCN-coordinated and pristine samples. (c) N_2 adsorption/desorption isotherms of TA-HK (pink) and TCM-HK (blue); for comparison, the isotherm of a pristine HKUST-1 sample evacuated at 25 °C is shown (black). Reproduced with permission from ref. 35, Copyright 2018, American Chemical Society.

and MeCN. The mechanism proceeds in two steps: the coordination exchange of the original solvent molecules with DCM, followed by the spontaneous dissociation of the weakly bound DCM at room temperature, which generates open Cu(II) sites. DCM treatment of HKUST-1 at room temperature yielded a surface area of ~2030 $m^2\,g^{-1}$, nearly identical to the ~2085 m^2 g^{-1} obtained by thermal activation. Raman spectroscopy confirmed the disappearance of Cu–Cu bands associated with EtOH and MeOH coordination (178 and 185 cm^{-1}), eventually shifting to 228 cm^{-1}, characteristic of fully activated Cu(II) sites. Crucially, the framework integrity was preserved perfectly, and comparable efficiencies were achieved for large-area MOF films, underscoring applicability and scalability.

This concept was extended to TCM.[35] Room-temperature TCM soaking of EtOH-HK, MeOH-HK, and MeCN-HK samples resulted in the complete removal of solvent after several cycles. Powder X-ray diffraction confirmed structural integrity, and N_2 adsorption gave a surface area of ~2035 $m^2\,g^{-1}$ (Fig. 16b and c). *In situ* Raman measurements directly captured the activation result (Fig. 4c).

Chemical activation is in particular advantageous for thermally unstable systems. In a mixed-matrix membrane composed of HKUST-1 and polyvinylidene fluoride, thermal treatment deformed the polymer phase and degraded the porosity, whereas TCM activation at ambient temperature preserved both the polymer morphology and the MOF porosity (Fig. 17).[35] This approach also succeeded for DUT-34 (also called MOF-143), which collapses irreversibly even under mild vacuum conditions at room temperature.[37] Sequential treatment with DCM or TCM removed precoordinated molecules, such as EtOH and DMF, without causing framework damage. Raman spectroscopy and *in situ* ^{1}H NMR confirmed solvent removal during treatment. Notably, DUT-34 crystals remained intact for more than 2 months after activation, demonstrating that chemical activation provides a safe and reliable alternative when thermal routes fail.

4.1.2 Gas-flow activation. Gas-flow activation also utilizes dynamic bonding at OMSs without solvent exchange.[39] Transiently dissociated molecules are continuously swept away by collisions with flowing inert gas (Fig. 18a). This approach avoids high-temperature heating and large volumes of weak donors, addressing limitations of chemical activation.

Efficacy was first evaluated on H_2O-HK, chosen for its well-defined Cu–Cu nodes and diagnostic Raman band. Under static conditions, complete activation required ~90 °C, with the Cu–Cu band shifting from 175 to 230 cm^{-1}. Under N_2 flow (50 mL min^{-1}), however, full activation was achieved at only ~40 °C within 5 min (Fig. 18b). At 25 °C, continuous N_2 flow for 120 min also produced the open-metal band at 230 cm^{-1}. These results demonstrate that N_2 flow substantially lowers the activation temperature by accelerating the removal of transiently dissociated molecules *via* collisions.

Because Ar atoms are heavier than N_2, Ar flow further enhances activation efficiency. For H_2O-HK, Ar reduced the activation temperature from 40 °C (under N_2 flow) to 25 °C, and for EtOH-HK, from 90 °C (under N_2 flow) to 60 °C (Fig. 18c). Bulk activation of EtOH-HK confirmed practicality: Ar-flow activation at 90 °C gave 1907 $m^2\,g^{-1}$, comparable to 1992 m^2 g^{-1} after thermal activation at 180 °C. At lower Ar-flow activation temperatures (25 and 40 °C), the internal surface areas were 948 and 1350 $m^2\,g^{-1}$, respectively, reflecting incomplete EtOH removal; however, increasing the Ar flow to 5 L min^{-1} at 25 °C increased the surface area to 1554 $m^2\,g^{-1}$, highlighting the role of collision energy. Thus, gas-flow activation exploits the intrinsic dynamic bonding at OMSs to achieve efficient and mild activation.

4.2 Solvent effect in MOF catalysis through dynamic weak coordination bonding

MOFs containing OMSs have emerged as highly promising heterogeneous catalysts owing to their ability to offer well-defined and accessible catalytically active metal centers. In such systems, catalytic activity is governed not only by the intrinsic nature of the metal sites but also by the surrounding solvent environment. Solvent molecules can coordinate to the OMSs, competing with catalytic substrates for binding and
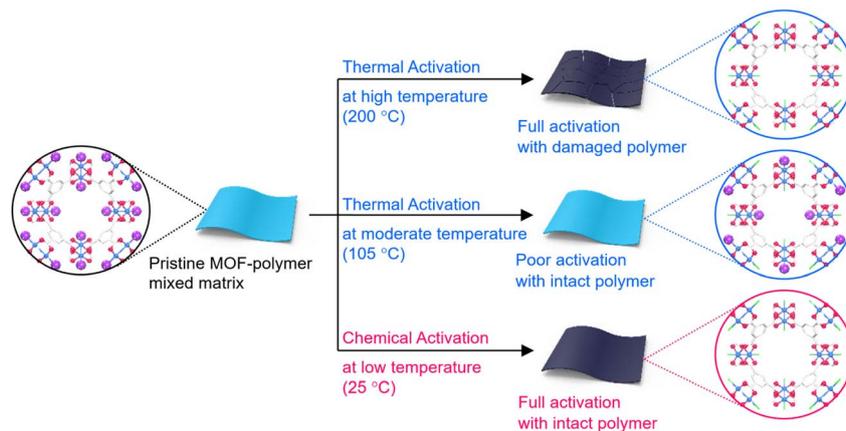
9100 | *J. Mater. Chem. A*, 2026, **14**, 9088–9114

This journal is © The Royal Society of Chemistry 2026

Fig. 17 Schematic comparison of activation routes for HKUST-1/polymer mixed matrices: thermal activation at high temperature (200 °C) achieves full activation but damages the polymer; thermal activation at moderate temperature (105 °C) preserves the polymer but provides poor activation; chemical activation with TCM at 25 °C affords full activation with an intact polymer. Hydrogen atoms bound to the carbon atoms in the benzene moieties are omitted for clarity. Reproduced with permission from ref. 35, Copyright 2018, American Chemical Society.

thereby modulating both accessibility and reactivity. Consequently, the balance between solvent coordination and substrate binding exerts a decisive influence on the catalytic performance of OMS-containing MOFs. Importantly, this competition is inherently dynamic—the coordination bonds at the OMSs are not static but can reversibly exchange between solvent molecules and substrate species under specific reaction conditions.

This dynamic behavior provides a mechanistic basis for understanding the solvent effect in MOF catalysis.[32] Weakly coordinating solvents such as DCM and TCM are particularly favourable, as their rapid association and dissociation at $Cu(\text{II})$ centers occur competitively with substrate molecules. This dynamic equilibrium keeps the OMSs accessible, sustaining catalytic activity throughout the reaction. In contrast, strongly coordinating solvents—including DMF, diethyl ether (DEE), and MeCN—bind tightly once coordinated and are not readily replaced by catalytic substrates, resulting in active-site blocking and diminished catalytic efficiency (Fig. 19a).

The critical role of dynamic bonding was clearly demonstrated in hydrogenation reactions of acetophenone and acetone using activated HKUST-1 as a model catalyst (Fig. 19b). In the hydrogenation of acetophenone, weakly coordinating solvents such as TCM, DCM, chlorobenzene (PhCl), and toluene (Tol) afforded high conversions of 96, 77, 64, and 74%, respectively. In contrast, reactions performed in strongly coordinating solvents—DMF, DEE, and MeCN—exhibited markedly reduced conversions of 30, 15, and 0%, respectively. A similar trend was observed in the hydrogenation of acetone (Fig. 19c): weakly coordinating solvents gave conversions of 96, 33, 36, and 51% for TCM, DCM, PhCl, and Tol, whereas strongly coordinating solvents yielded only 12, 11, and 7% for DMF, DEE, and MeCN. These comparative results compellingly demonstrate that catalytic performance is maximized under weak dynamic coordination, where the metal centers remain in a continually open and reactive state.

Therefore, the surrounding solvent environment plays a direct and decisive role in regulating the accessibility of OMSs.

Weakly coordinating solvents, by maintaining a reversible equilibrium at the coordination interface, promote sustained activity and efficient catalysis. This relationship underscores the fundamental importance of dynamic coordination bonding in optimizing catalytic function in OMS-containing MOFs.

4.3 Gas adsorption enabled by dynamic metal–guest molecule bonding

In amine-grafted MOFs, dynamic metal–guest bonding is the key mechanistic driver of cooperative gas uptake. These frameworks—most notably the expanded-pore $M_2(\text{dobpdc})$ $\{\text{dobpdc}^{4-} = 4,4'\text{-dioxidobiphenyl-}3,3'\text{-dicarboxylate}\}$ family— are post-synthetically modified with diamines such that one amine terminus coordinates to an OMS while the other points into the pore.[76–80] This arrangement furnishes a dense array of uniform, accessible Lewis-basic sites for acidic gases (*e.g.*, CO_2 and CS_2) and enables cooperative adsorption *via* dynamic coordination exchange: upon gas dosing, reversible association–dissociation events at the metal center mediate substitution between metal–amine and metal–gas adducts, propagating ordered binding motifs along the channels. In this way, adsorption is amplified beyond simple physisorption, with the dynamic equilibria at OMSs dictating uptake pressure, capacity, and regenerability.

4.3.1 CO_2 adsorption at amine-grafted MOFs. Global warming, driven by sustained reliance on fossil fuels, has elevated CO_2 to the primary greenhouse gas of concern.[81–84] To mitigate these impacts, porous materials—particularly MOFs— have attracted intense interest as platforms for CO_2 capture.[85–87] Among them, amine-grafted MOFs stand out because they harness dynamic coordination bondings during both adsorption and desorption. Their remarkable performance originates from a cooperative chemisorption pathway: upon CO_2 exposure, the grafted amine reacts to form a carbamate species. This transformation proceeds *via* dissociation of the original metal–amine coordination, followed by formation of a new metal–carboxylate bond associated with the carbamate, which then
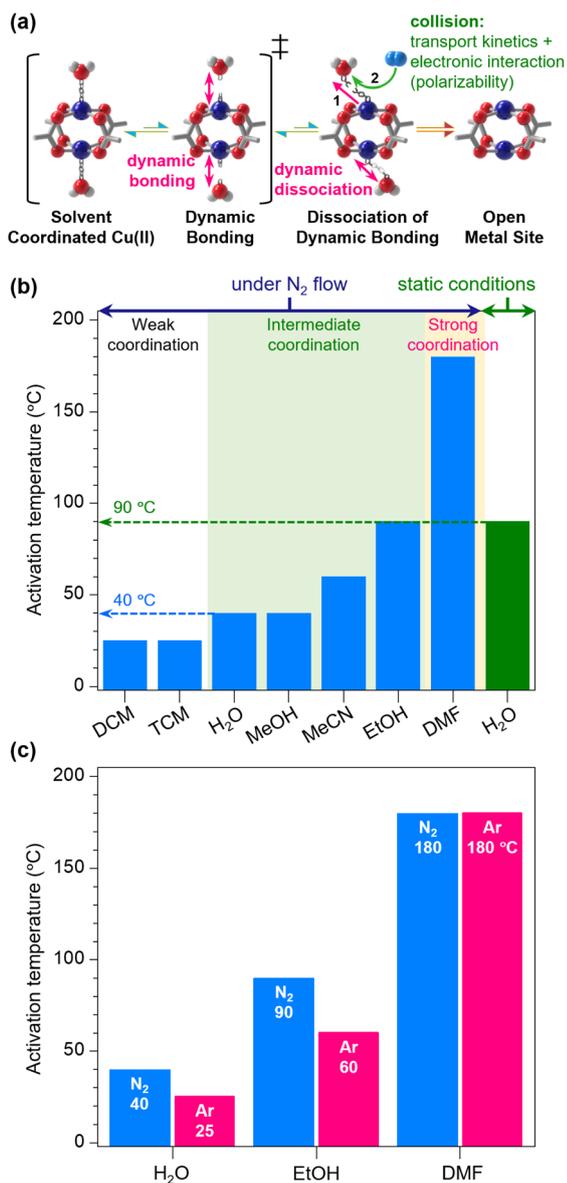
This journal is © The Royal Society of Chemistry 2026

J. Mater. Chem. A, 2026, **14**, 9088–9114 | **9101**

Fig. 18 (a) Schematic representation of dynamic dissociation of coordinating H_2O at Cu(II) centers, emphasizing the roles of collision kinetics and electronic interactions with flowing N_2. (b) Activation temperatures determined by in situ Raman spectroscopy under N_2 flow (blue) versus static conditions (green) for various solvents; notably, H_2O-HK shifts from 90 °C (static) to 40 °C (N_2 flow). (c) Activation temperatures for H_2O-, EtOH-, and DMF-coordinated HKUST-1 under N_2 (blue) and Ar (pink) flows, showing the greater efficiency of Ar. Reproduced with permission from ref. 39, Copyright 2025, Royal Society of Chemistry.
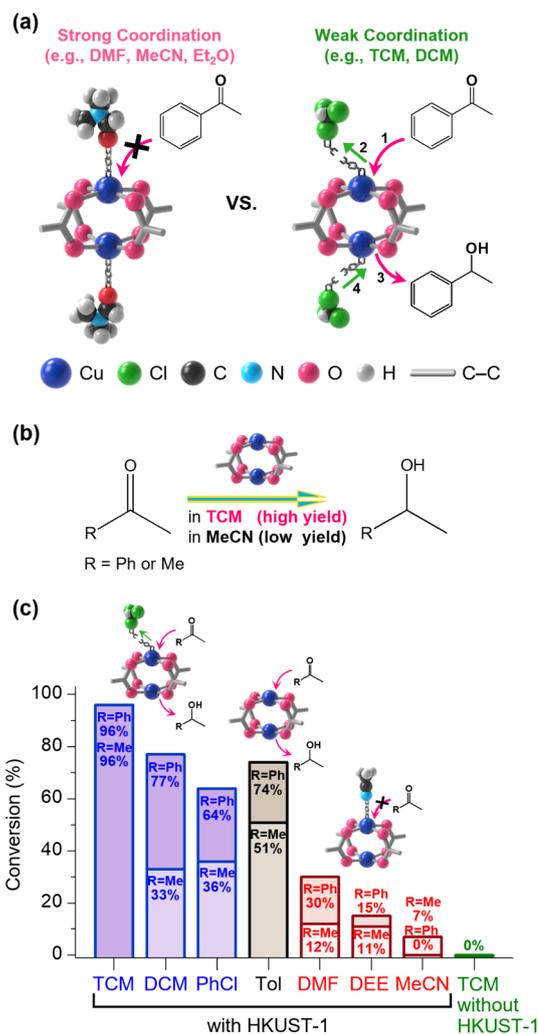

Fig. 19 (a) Schematic hypothesis for solvent effects: weakly coordinating solvents (e.g., TCM and DCM) permit reversible access of substrates to Cu(II) centers, whereas strongly coordinating solvents (e.g., DMF, MeCN, and DEE) block active sites. (b) Scheme of acetophenone/acetone hydrogenation catalyzed by Act-HK. (c) Conversion profiles for reactions conducted in TCM, DCM, and PhCl (blue), Tol (black), DMF/DEE/MeCN (red) with Act-HK, and in TCM without HKUST-1 (green), highlighting superior performance in weakly coordinating media. Reproduced with permission from ref. 32, Copyright 2022, Royal Society of Chemistry.

propagates into ammonium-carbamate chains (Fig. 20a). The cooperative coordination exchange thus demonstrates that the initial metal–amine bond is not static but is reversibly replaced by coordination to CO_2.

In 2015, the Long group first established this cooperative exchange mechanism using mmen-M_2(dobpdc), where mmen = N,N′-dimethylethylenediamine.[88] Rietveld refinement of powder X-ray diffraction data provided a structural basis: prior

to CO_2 dosing, the diamine coordinates to the metal through one amine end, with a metal–amine distance of 2.29(6) Å (Fig. 20b), while the second amine projects into the channel. After CO_2 uptake, carbamate formation is evidenced by a metal–oxygen bond at 2.10(2) Å (Fig. 20c and d) and an N···O interaction of 2.61(9) Å between the carbamate O atom and the neighboring diamine N atom. Importantly, the ordered chain motif persists at 295 K, indicating that CO_2 adsorption at room temperature induces a framework-level structural transition governed by dynamic coordination bonding.

Spectroscopic measurements further corroborate this mechanism. In the IR spectra, the N–H stretches at 3350 and 3250 cm^{-1} broaden and red-shift at 30 °C, reflecting

9102 | J. Mater. Chem. A, 2026, 14, 9088–9114

This journal is © The Royal Society of Chemistry 2026

ammonium formation stabilized by hydrogen bonding (Fig. 20e). Upon heating, the carbamate decomposes to regenerate free amines: N–H bands sharpen, intensify, and blue-shift, consistent with stronger N–H bonds. Concurrently, a band near 1650 cm^{-1} (carbamate C=O stretch) emerges at low temperature and diminishes with heating; the 1335 cm^{-1} feature (carbamate C–N stretch) follows the same trend. These temperature-dependent IR signatures provide direct evidence for a reversible amine–carbamate equilibrium driven by coordination exchange between M–N and M–O bonds during CO_2 adsorption and desorption.

Building on this cooperative picture, the CO_2 sorption behavior of mmen-M_2(dobpdc) was examined across metals (M = Mg, Mn, Fe, Co, Zn) to elucidate metal-dependent effects. Among these, mmen-Mg_2(dobpdc) exhibits the highest uptake and strongest affinity, approaching the theoretical limit of one CO_2 per diamine, with working capacities surpassing that of aqueous amines under mild regeneration. A hallmark of these materials is the step-shaped isotherm, rarely seen in other sorbents and attributed to cooperativity: adsorption increases sharply within a narrow pressure window, enabling efficient capture. Upon heating, the step shifts to higher pressures, allowing large working capacities with only modest temperature swings.

Because chemisorption stoichiometry typically limits capacity to ~1 equivalent of CO_2 per diamine,[78–80,88] molecular design has been used to surpass this ceiling. Introducing a bulky primary/tertiary (1°/3°) diamine, 1-(2-aminoethyl) piperidine (pip2), into Mg_2(dobpdc) yields capacities up to 1.5 equivalents per diamine molecule via a mixed chemisorption–physisorption mode (Fig. 21a).[89] As before, CO_2 reacts to form carbamates in a 1:1 chemisorptive ratio with metal sites; additionally, steric repulsion from pip2 expands spacing between adjacent carbamates, generating voids that accommodate extra CO_2 by physisorption (Fig. 21b). The result showed an exceptional capacity (~5 mmol g^{-1}). Cycling and breakthrough tests confirm structural robustness through sequential cooperative adsorption, showcasing mixed mechanisms as a route to exceed conventional limits.

For practical deployment—characterized by higher partial pressures and humid streams[90,91]—amine-grafted MOFs must shift the step to higher pressures and exhibit strong hydrolytic stability. To this end, the Long group developed a pore-expanded framework, Mg_2(olz) {olz^{4-} = (E)-5,5′-(diazene-1,2-diyl)bis(2-oxidobenzoate)}, which accommodates bulky primary/secondary (1°/2°) diamines such as N,N-diethylethylenediamine (ee-2) without steric penalty (Fig. 21c and d).[92] The steric bulkiness of ee-2 weakens inter-chain cooperativity, shifting the steep uptake step to higher CO_2 pressures aligned with industrial conditions. Simultaneously, increased pore hydrophobicity reduces competitive H_2O adsorption, enhancing stability under humidity. Consequently, ee-2-Mg_2(olz) captures >90% of CO_2 from flue gas with a high working capacity (3.9 mmol g^{-1}) and low regeneration energy (2.15 MJ kg^{-1}), maintaining performance over 1000 cycles.

4.3.2 CS$_2$ adsorption in amine-grafted MOFs. Dynamic coordination bonding similarly enables efficient CS_2 capture.[93] Analogous to the CO_2 mechanism, the grafted amine reacts with
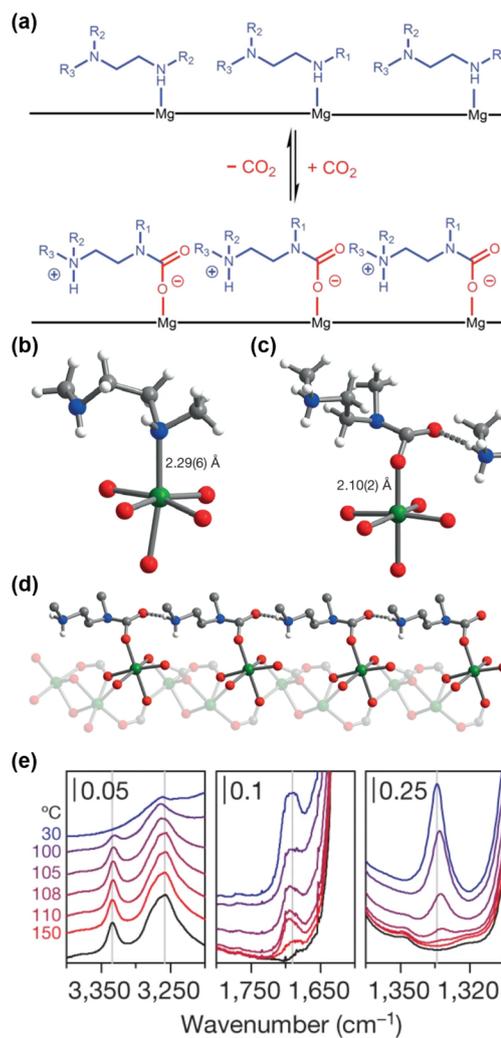

Fig. 20 (a) Depiction of cooperative CO_2 adsorption in amine–Mg_2(dobpdc) forming ammonium–carbamate chains. Reproduced with permission from ref. 89, Copyright 2024, American Chemical Society. (b and c) Portions of the crystal structures of mmen-Mn_2(dobpdc) before (b; M–N = 2.29(6) Å) and after (c; M–O = 2.10(2) Å) CO_2 adsorption, evidencing metal–amine to metal–carbamate substitution. (d) Final configuration showing an ammonium–carbamate chain propagating along the pore surface (Mn, C, O, N, and H are shown in green, grey, red, blue, and white; some H omitted for clarity). (e) Infrared spectra of mmen-Mg_2(dobpdc) upon dosing 5% CO_2 in N_2 and cooling from 150 to 30 °C, highlighting N–H (left), C=O (center), and C–N (right) stretching vibration regions. Reproduced with permission from ref. 88, Copyright 2015, Springer Nature.

CS_2 to form a dithiocarbamate species (Fig. 22a), involving dissociation of the metal–amine bond followed by formation of a new metal–dithiocarbamate linkage. SCXRD establishes this pathway: before CS_2 exposure, the diamine coordinates to Zn through one amine group (Zn–N = 2.182(4) Å; Fig. 22b), with the second amine oriented into the pore. After CS_2 adsorption, a monodentate Zn–S bond at 2.483(1) Å is observed, propagating into ordered chains.

IR spectroscopy corroborates the structural assignment. Upon CS_2 dosing, two new bands at 961 and 949 cm^{-1} (C–S
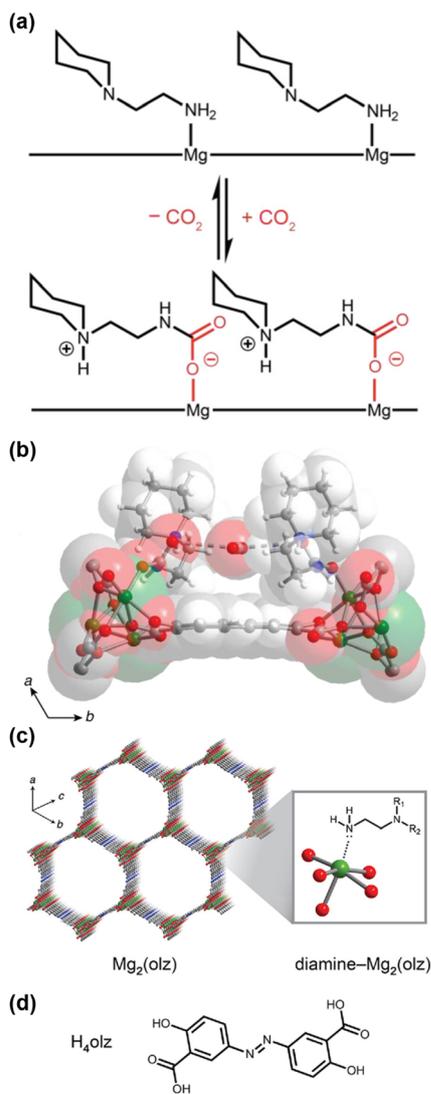
This journal is © The Royal Society of Chemistry 2026

J. Mater. Chem. A, 2026, **14**, 9088–9114 | 9103

Fig. 21 (a) Illustration of the proposed mechanism of CO_2 chemisorption in pip2-Mg$_2$(dobpdc), forming ammonium–carbamate pairs. (b) Rietveld-refined structure of $(CO_2)_{1.5}$-pip2-Mg$_2$(dobpdc) viewed in the ab plane. Reproduced with permission from ref. 89, Copyright 2024, American Chemical Society. (c) Structure of activated Mg$_2$(olz) and its post-synthetic amination to give diamine–Mg$_2$(olz) (Mg, O, N, C, and H are shown in green, red, blue, gray, and white). (d) Structure of the H$_4$olz linker. Reproduced with permission from ref. 92, Copyright 2023, American Chemical Society.

stretches), absent in the pristine MOF, appear (Fig. 22c), consistent with the replacement of Zn–N by Zn–S bonding and the formation of dithiocarbamate species. Additional features at 1343 and 1318 cm^{-1} (C–N stretching) indicate close interactions between the dithiocarbamate moiety and neighboring amines within the channels. These spectral changes collectively evidence a coordination-exchange process wherein Zn–N bonds are replaced by Zn–S bonds while new C–N linkages form. Guided by this mechanism, adsorption studies show that in mm-2-Mg$_2$(dobpdc) {mm-2 = 1°/3° diamine *N*,*N*-dimethylethylenediamine}, CS$_2$ is taken up cooperatively with a sharp step at 5 mbar and a saturation
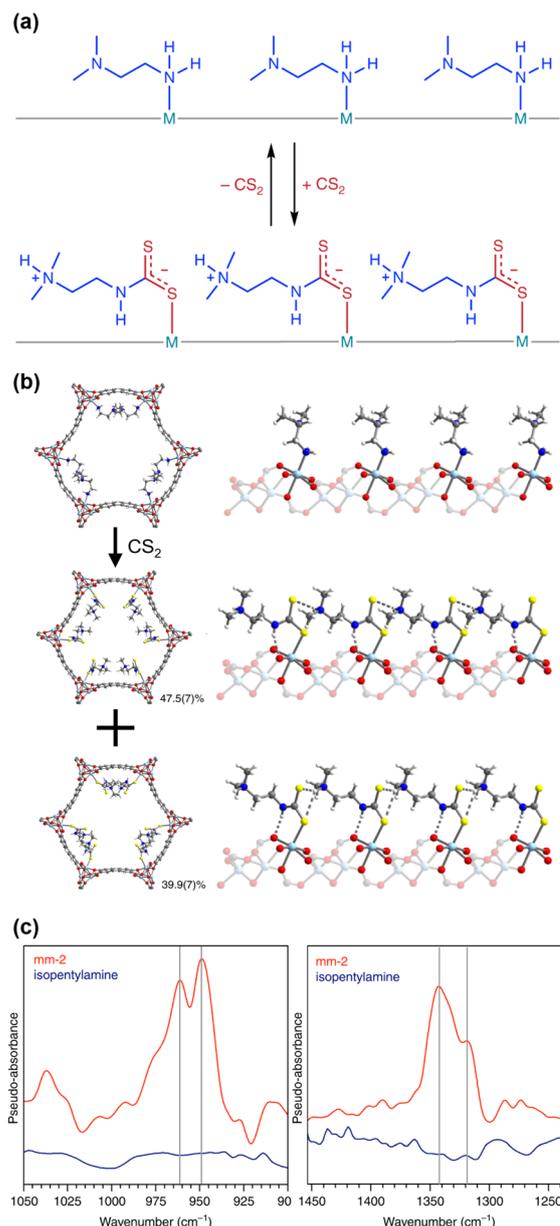
Fig. 22 (a) Proposed reversible mechanism for cooperative CS$_2$ adsorption in mm-2-M$_2$(dobpdc): insertion of CS$_2$ into M–N bonds, proton transfer, and formation of paired ammonium dithiocarbamate chains. (b) Portions of the mm-2-Zn$_2$(dobpdc) structure (left, diamines coordinated to Zn(II)) and CS$_2$-inserted mm-2-Zn$_2$(dobpdc) (right), showing two coexisting chain conformations; Zn, N, O, C, S, and H are shown in light blue, blue, red, gray, yellow, and white, respectively. (c) *In situ* diffuse-reflectance FT-IR spectra upon exposing activated mm-2-Mg$_2$(dobpdc) and isopentylamine–Mg$_2$(dobpdc) to CS$_2$ vapor at 25 °C. Reproduced with permission from ref. 93, Copyright 2018, Springer Nature.

capacity of 8 mmol g^{-1} at 25 °C, delivering working capacities of 7.4 mmol g^{-1} under temperature swings—significantly outperforming zeolites.[94]

Overall, amine-grafted MOFs achieve high efficiencies by leveraging reversible coordination exchange of metal–amine bonds at OMSs, enabling cooperative uptake rather than simple

9104 | *J. Mater. Chem. A*, 2026, **14**, 9088–9114

This journal is © The Royal Society of Chemistry 2026

physisorption. These observations firmly establish dynamic bonding as the key mechanistic feature underlying the exceptional gas-adsorption performance of amine-grafted MOFs.

5 Application of metal–linker dynamic bonding

Dynamic metal–linker bonding extends beyond a fundamental concept to provide a mechanistic basis for diverse MOF applications. For instance, (5.1) transient bond dissociation enables catalytic reactivity even in fully coordinated frameworks. (5.2) Liquid and glassy MOFs can arise from dynamic, structure-preserving reorganizations that retain metal–linker connectivity. (5.3) In addition, guest-induced generation of transient OMSs facilitates gas sorption. Collectively, these examples establish metal–linker bond dynamics as a key lever for designing MOFs for catalysis, glass formation, and gas adsorption.

5.1 Hemilabile MOF catalysts *via* dynamic metal–linker bonding

The dynamic nature of metal–linker coordination bonds can open alternative catalytic pathways even when metal sites are fully coordinated. Catalytic activity emerges when thermal energy or guest molecules (see Sections 3.1 and 3.3) drive

temporary excursions to dissociated states, transiently exposing reactive metal centers for catalytic substrate binding. In this open state, catalysis proceeds at the exposed metal, followed by product release and reassociation of the linker to the metal without permanent structural deformation. Notably, dynamic bonding can endow MOFs without OMSs with catalytic function while often offering greater structural robustness than OMS-containing MOFs.

In 2010, the Van Der Voort group introduced the concept of catalysis *via* dynamic metal–linker coordination, showing that a vanadium-based MOF, V-MIL-47, catalyzes olefin oxidation despite the absence of OMSs.[27] V-MIL-47 consists of $V(IV)O_6$ octahedra connected by terephthalate linkers into one-dimensional chains; in principle, the fully six-coordinated vanadium centers provide no vacant sites for catalytic substrates. Nevertheless, V-MIL-47 catalyzed the oxidation of cyclohexene using 70 wt% *tert*-butyl hydroperoxide (TBHP) in water as the oxidant. The reaction proceeds at instantaneously formed defect sites, where transient metal–linker dissociation allows substrate binding and enables subsequent oxidation. Calculations further indicated that TBHP can induce metal–linker dynamics, thereby facilitating oxidation. Dynamic coordination bonding has since been extended to highly stable Zr-based frameworks. Van Speybroeck and coworkers demonstrated that UiO-66 catalyzes Oppenauer oxidation,[28] wherein heating UiO-66 to 120 °C reduces the Zr coordination number
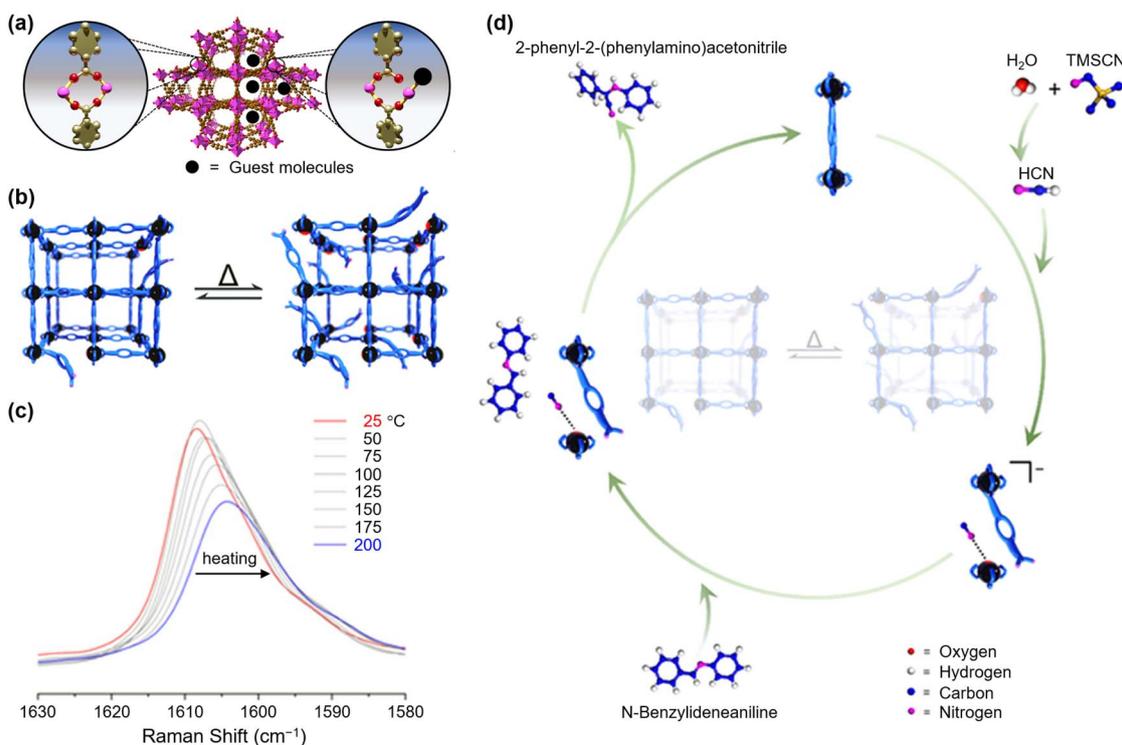
Fig. 23 (a) Illustration of hemilabile metal–ligand bond dynamics upon guest adsorption in MFM-300(Sc). Reproduced with permission from ref. 95, Copyright 2022, Wiley, VCH. (b) Representation of transient OMSs generated by hemilabile bonds and poised for catalysis at low and high temperatures. (c) Variable temperature-resonance Raman spectra of MFM-300(In) from 200 to 25 °C, showing temperature-dependent shifts consistent with partial linker dissociation. (d) Proposed catalytic cycle for forming 2-phenyl-2-(phenylamino)acetonitrile driven by hemilabile linker dynamics in MFM-300(In) (C, blue; H, white; N, pink; O, red; S, yellow; In, black). Reproduced with permission from ref. 31, Copyright 2023, American Chemical Society.

This journal is © The Royal Society of Chemistry 2026

J. Mater. Chem. A, 2026, **14**, 9088–9114 | **9105**

Fig. 24 (a) Schematic illustration of the principle of MOF melting: when the melting temperature (T_m) lies below the decomposition temperature (T_d), transient metal–ligand bond cleavage enables conversion to a liquid/glass; if $T_m > T_d$, ligand decomposition prevents melting. Reproduced with permission 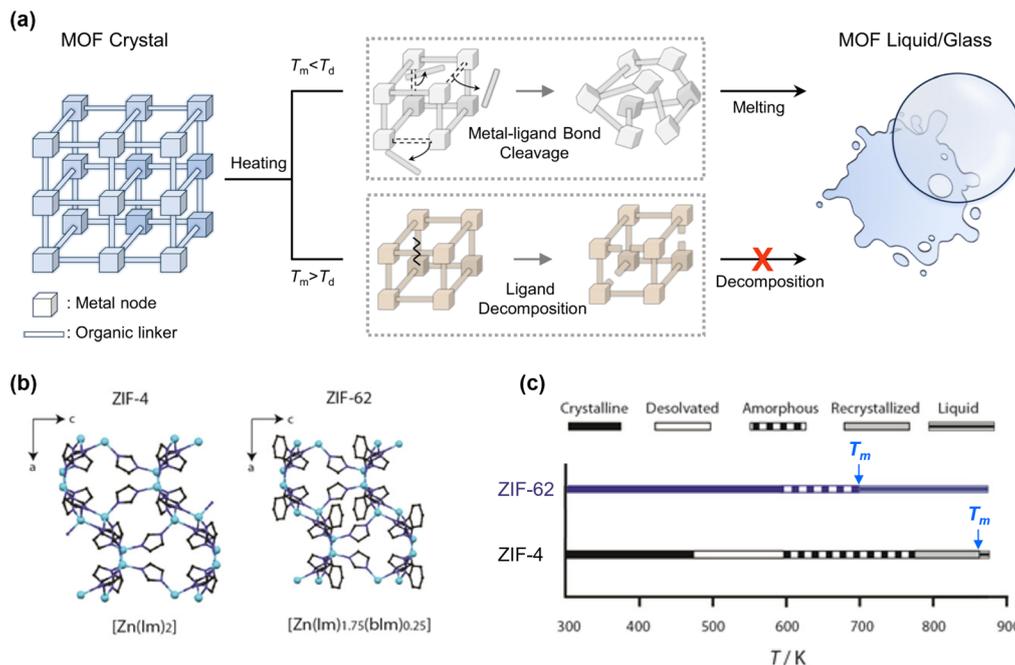from ref. 115, Copyright 2024, Springer Nature. (b) Unit cells of ZIF-4 and ZIF-62 viewed along the b axis (N, dark blue; Zn, light blue; C, black; H omitted). (c) Schematic thermal evolution upon heating, highlighting that ZIF-62 amorphizes on desolvation and exhibits a wide window between melting and framework decomposition. Reproduced with permission from ref. 112, Copyright 2016, American Chemical Society.

from 8 to 6 *via* transient dissociation of one BDC (benzene-1,4-dicarboxylic acid) linker, generating defect sites that function as catalytic centers. These studies highlight dynamic bonding as a core mechanism enabling catalysis in MOFs that lack permanent OMSs.

Based on these observations, recent efforts have moved from post hoc explanation to rational design of new frameworks that purposefully harness dynamic bonding to enhance catalysis. A representative case is MFM-300(Sc) {Sc$_2$(OH)$_2$(L), L = biphenyl-3,3′,5,5′-tetracarboxylate}, where Sc(III) centers are octahedrally coordinated to four carboxylates and two μ$_2$-OH groups.[29] In this MOF, saturated Sc(III) centers become a catalytically active component when dynamic bonding generates hemilabile Sc–(O)OC linkages, permitting reactant binding and turnover (Fig. 23a). VT-DRIFTS provided direct evidence of this behavior, showing continuous shifts in stretching vibrational frequencies of carboxylate upon guest-induced coordination exchange. Capitalizing on this property, Maurin and coworkers showed that MFM-300(Sc) catalyzes the Strecker reaction of *N*-benzylideneaniline with trimethylsilyl cyanide (TMSCN) with excellent recyclability, maintaining crystallinity and activity over 5 cycles.[95] DFT calculations supported a mechanism involving transient coordination of HCN at Sc(III) centers.

The isostructural MFM-300(In) exhibits comparable dynamics and catalyzes the same Strecker reaction (Fig. 23b).[31] Variable-temperature resonance Raman spectroscopy performed at 25–200 °C revealed slight red shifts of the COO$^-$ bands from 1608 to 1602 cm^{-1}, consistent with partial metal–

linker dissociation and the generation of transient OMSs (Fig. 23c). Catalytic performance mirrored spectroscopy: conversion increased from 41% at room temperature to 93% at 55 °C, in line with thermally enhanced dynamicity. A mechanistic picture was proposed: HCN deprotonation generates CN$^-$ and H$^+$ species; CN$^-$ dynamically substitutes carboxylate at transiently opened In(III) sites, while H$^+$ protonates *N*-benzylideneaniline to form an iminium ion. Nucleophilic attack by CN$^-$ on iminium yields 2-phenyl-2-(phenylamino) acetonitrile as the product (Fig. 23d).

Gao and coworkers reported a Cd-based framework, Cd(TPPA)I$_2$ {TPPA = tris[4-(pyridin-3-yl)phenyl]amine}.[30] The structure features tetrahedral Cd(II) nodes coordinated by TPPA *N*-donors and iodide; π–π interactions assemble one-dimensional chains into two-dimensional sheets. Open channels expose pyridylamine and pyridine groups as Lewis-basic sites, while labile Cd–I bonds provide hemilabile sites for catalysis. This dual-site motif enables efficient cycloaddition of CO$_2$ with epoxides to form cyclic carbonates. Microcalorimetry, X-ray photoelectron spectroscopy, fluorescence spectroscopy, and DFT calculations together indicate a cycle in which epoxides coordinate to Cd(II), transiently dissociating iodide to generate a pseudo-pentacoordinate intermediate. The liberated I$^-$ nucleophilically attacks the epoxide to form an alkoxide, which then reacts with CO$_2$ to yield cyclic carbonates, regenerating I$^-$. In this mechanistic pathway, dynamic Cd–I bond cleavage lowers the barrier of the rate-determining step,
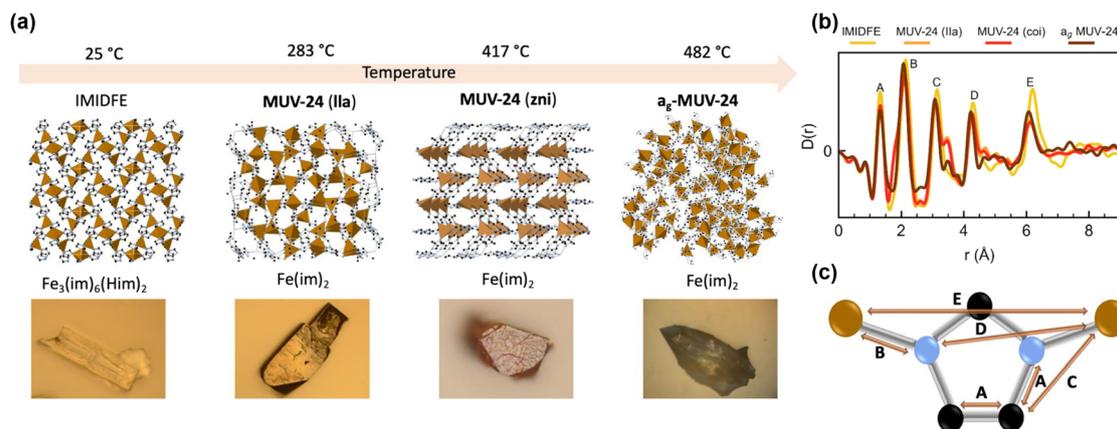
9106 | *J. Mater. Chem. A*, 2026, **14**, 9088–9114

This journal is © The Royal Society of Chemistry 2026

Fig. 25 (a) Temperature-driven phase evolution of IMIDFE to MUV-24 (lla), MUV-24 (zni), and finally the amorphous glass a_g-MUV-24 (schematic), with the corresponding optical micrographs; vitrification is observed in the final material. (b) X-ray pair distribution functions, D(r), for IMIDFE, MUV-24 (lla), MUV-24 (coi), and a_g-MUV-24, showing retention of short-range order across phases. (c) Structural representation assigning short-range bonds/pair distances (Fe, brown; C, black; N, blue) to the labeled X-ray pair distribution peaks. Reproduced with permission from ref. 113, Copyright 2023, American Chemical Society.

illustrating how dynamic coordination can be engineered to boost catalytic activity.

5.2 MOF liquids and glasses derived from dynamic coordination

Despite major advances in crystalline MOFs, industrial deployment remains hampered by grain boundaries between crystallites.[96,97] Strategies to mitigate this limitation include binding MOF powders with polymers,[98,99] shaping into beads or pellets,[100–102] and growing larger crystals *via* using modulators.[103–106] Recently, meltable crystalline materials—particularly glassy MOFs—have attracted attention as a promising route to circumvent grain boundaries.[107] Glassy MOFs are amorphous coordination polymers obtained by melting crystalline MOFs while preserving metal–linker connectivity despite the loss of long-range order. Formation requires the melting

temperature to lie below the decomposition temperature (Fig. 24a).[48–50] Although most MOFs decompose upon heating, a subset satisfies this criterion. These meltable MOFs undergo reversible transformations to glassy states in which metal–linker bonds dissociate and reassociate at adjacent sites, forming new linkages through dynamic metal–linker coordination.

Early studies focused on zeolitic imidazolate frameworks (ZIFs), whose intrinsically weaker metal–imidazolate coordination and rapid dynamics favor melting. Building on ZIFs with varied network topologies, framework densities, porosities, and linker functionalities,[108,109] systematic investigations correlated their structure with glass-transition behavior and liquid/glass formation. For example, electron-withdrawing substituents on imidazolate linkers (*e.g.*, cyano and halogen) lower the glass transition temperature, consistent with weakened coordination arising from
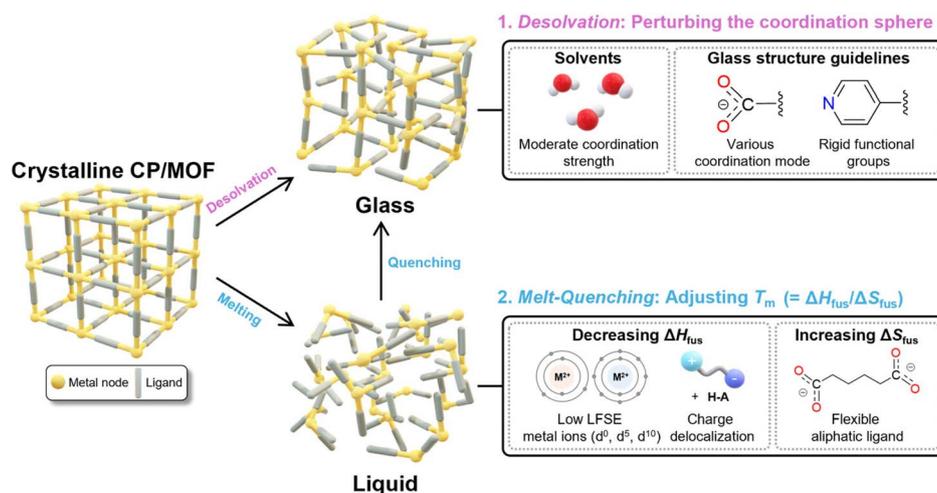
Fig. 26 Schematic strategies for preparing carboxylate-based MOF glasses and design guidelines for practical use. Two routes are highlighted: (1) desolvation to perturb the coordination sphere and generate disorder (moderate-strength solvents; preferred coordination modes/rigid groups), and (2) melt-quenching by tuning $T_m = \Delta H_{fus}/\Delta S_{fus}$ (decreasing ΔH_{fus} *via* low-LFSE metal ions and charge delocalization; increasing ΔS_{fus} *via* flexible aliphatic linkers). Reproduced with permission from ref. 50, Copyright 2024, American Chemical Society.

This journal is © The Royal Society of Chemistry 2026

J. Mater. Chem. A, 2026, **14**, 9088–9114 | **9107**

reduced electron density.[63,110,111] Steric effects were probed by partially substituting imidazole (im) with bulkier benzimidazole (bim) in ZIF-4 to yield $Zn(im)_{2-x}(bim)_x$ (Fig. 24b). The introduction of bulky groups lowers the melting temperature (Fig. 24c), reflecting weakened coordination due to steric hindrance.[112]

Beyond linker functionality, the metal node is a decisive parameter. While glassy ZIFs have largely involved Zn, the Espallargas group reported the first Fe(II)-based glassy ZIF, denoted as IMIDFE.[113] IMIDFE exhibits a lower glass transition temperature (190 °C) than ZIF-4 (292 °C) with the same topology,[114] suggesting that metal substitution is an effective lever for tuning thermal transitions via metal–linker dynamicity. Thermogravimetric analysis, differential scanning calorimetry, and SCXRD confirmed phase evolution: upon heating to 283 °C, IMIDFE converts to MUV-24 (lla) via imidazole removal; subsequent heating to 471 °C yields MUV-24 (zni); and further heating to 482 °C produces an amorphous glass, a_g-MUV-24 (Fig. 25a). X-ray pair distribution function analysis, which reports short-range distances, verified retention of local metal–linker environments, as peak positions remain unchanged across the transition (Fig. 25b and c).

Azolate linkers thus provide a fertile platform for glassy MOFs owing to relatively weak coordination and high thermal stability. By contrast, carboxylate-based glassy MOFs are challenging: strong metal–carboxylate bonds typically trigger decomposition before melting. Moon and coworkers first realized carboxylate-based glassy MOFs using aliphatic linkers with Mg and Mn nodes.[115] Two design principles lowered the effective glass transition: (i) selecting metals with symmetric electron configurations—Mg(II) (d^0) and Mn(II) (d^5)—to reduce crystal field stabilization and weaken metal–linker bonding; and (ii) introducing aliphatic linkers to enhance conformational freedom in the liquid, providing an entropic advantage over aromatic linkers (Fig. 26). The increased liquid-phase entropy narrows the free-energy gap between solid and liquid, thus lowering glass transition temperature. These strategies established a conceptual blueprint for carboxylate glasses. Notably, the resulting materials displayed superior mechanical strength; for example, Mg-adp showed a hardness of 1.18 GPa and an elastic modulus of 18.29 GPa—both higher than those of previously reported glassy MOFs.[116,117]

Although several glassy MOFs are now known, many frameworks lack glass formation because organic linkers decompose before melting at high temperatures. Recent studies demonstrate that mechanical routes at lower temperatures can access the glassy state without thermal decomposition. External mechanical energy enhances metal–linker dynamicity, enabling amorphization at reduced temperatures. For instance, UiO-66 undergoes amorphization by ball milling, evidencing mechanically induced metal–linker dynamics.[118] Here, the crystal transforms into an amorphous phase while retaining metal–linker connectivity—analogous to thermal glass transitions. Similarly, applying high pressure (1.9 GPa) induces amorphization via partial carboxylate dissociation.[119] These findings underscore that mechanical stimuli such as ball milling and pressure can promote coordination dynamics and thereby facilitate glass formation.

Most research to date has centered on melting behavior and connectivity retention; however, directly correlating metal–linker bond dynamics with glass formation remains challenging. Horike and coworkers addressed this gap using ultra-fast solid-state magic-angle spinning ^{19}F NMR.[120] They compared $Zn(SiF_6)(bpp)_2$ and $Zn(TiF_6)(bpp)_2$ {bpp = 1,3-bis(4-pyridyl)propane}, each comprising octahedral Zn nodes bridged by flexible bpp linkers and XF_6^{2-} anions. The solid-state NMR data support a mechanism in which metal–linker dynamicity proceeds through sequential Zn–F bond dissociation and reassociation. Specifically, dissociation initiates an anion-rotation process; the XF_6^{2-} unit then rotates and reassociates with Zn, consistent with dynamic bonding. The Zn–F exchange rates were quantified as 3×10^4 s^{-1} for Zn–SiF$_6$ and 3.1×10^2 s^{-1} for Zn–TiF$_6$, evidencing markedly higher dynamicity in $Zn(SiF_6)(bpp)_2$. This trend aligns with Zn–F bond lengths—2.168(8) Å for $Zn(SiF_6)(bpp)_2$ versus 2.1408(8) Å for $Zn(TiF_6)(bpp)_2$—where longer bonds correlate with increased dynamics due to weaker interactions. Consistently, ball-milling tests revealed higher glass formability for $Zn(SiF_6)(bpp)_2$, providing direct evidence that metal–linker dynamicity is intimately linked to glass-transition behavior.

5.3 Gas adsorption facilitated by dynamic metal–linker bonding

The dynamic nature of metal–linker bonds has emerged as a key concept for understanding gas adsorption in MOFs. Mechanistically, guest molecules such as NH_3 or CO_2 can weaken metal–linker interactions, promoting partial bond dissociation and the transient generation of OMSs, at which the gas molecules subsequently coordinate (see Section 3.3).

5.3.1 NH_3 adsorption through partial bond dissociation. In 2021, the Maurin group demonstrated that NH_3 adsorption arises at the metal nodes of MFM-300(Sc), despite Sc(III) centers being fully coordinated to the linker.[29] Adsorption proceeds by inducing partial dissociation of the Sc–carboxylate bond, followed by Sc–NH_3 coordination. DFT calculations indicate that NH_3 first binds at the μ-O–H site and then migrates to a neighboring Sc(III) center, triggering partial Sc–carboxylate dissociation. The dissociated O atom forms a hydrogen bond with a nearby μ-O–H group, and this bond dynamicity permits NH_3 to coordinate at Sc(III) (Fig. 27a). DRIFTS provided convergent evidence: the COO$^-$ stretching vibrational bands at 1740 and 1727 cm^{-1} increase in intensity as NH_3 uptake proceeds, consistent with partial linker dissociation from the metal center (Fig. 27b). The Sc(III)–N rocking band at 840 cm^{-1} also intensifies, confirming Sc–NH_3 coordination (Fig. 27c). In parallel, the μ-O–H stretching band at 3683 cm^{-1} broadens with NH_3 dosing, evidencing hydrogen bonding between μ-O–H and the dissociated carboxylate (Fig. 27d). Together, these data show that NH_3 uptake occurs via partial metal–linker bond cleavage and subsequent NH_3 coordination at transiently formed OMSs. In accordance with this mechanism, the isotherm exhibits a sharp low-pressure step, and uptake increases to 13.1 mmol g^{-1} at 1 bar, indicating strong affinity of MFM-300(Sc) for NH_3. The capacity was retained over five cycles, confirming

9108 | J. Mater. Chem. A, 2026, **14**, 9088–9114

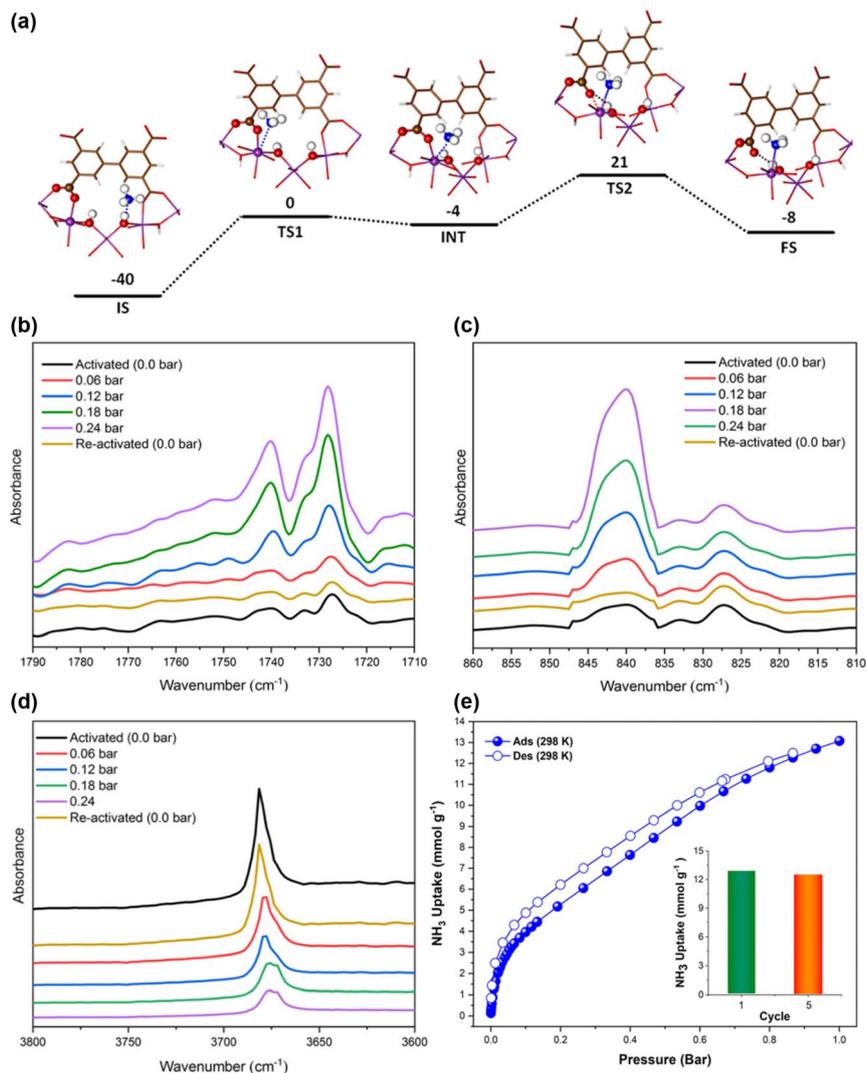This journal is © The Royal Society of Chemistry 2026

Fig. 27 (a) DFT-simulated potential energy profile for NH_3-triggered Sc−carboxylate dynamic bonding in MFM-300(Sc), showing the initial state (IS), transition states (TS1 and TS2), intermediate (INT), and final state (FS). Color code: C (brown), O (red), N (blue), H (white), and Sc (purple); energies in kJ mol^{-1}. (b–d) DRIFTS of NH_3 dosed over activated MFM-300(Sc) at 298 K and 0–0.24 bar, shown for (b) 1790–1710 cm^{-1}, (c) 860–810 cm^{-1}, and (d) 3800–3600 cm^{-1} regions. (e) NH_3 adsorption (filled blue) and desorption (open blue) isotherms at 298 K up to 1 bar; inset compares uptake in the 1st and 5th cycles. Reproduced with permission from ref. 29, Copyright 2021, American Chemical Society.

reversibility and the pivotal role of partial bond dissociation in repeated NH_3 sorption (Fig. 27e).

Consistent with this concept, the Long group showed that Cu(cyhdc) {cyhdc^{2-} = *trans*-1,4-cyclohexanedicarboxylate} exhibits exceptionally high NH_3 uptake by creating OMSs *via* partial bond dissociation.[2] Topologically, each Cu(II) in Cu(cyhdc) is coordinated by four equatorial carboxylate O atoms and one axial carboxylate O from a neighboring paddlewheel (Fig. 28a). Upon NH_3 exposure, partial dissociation at two equatorial and one axial carboxylate O atom enables coordination of four NH_3 molecules per Cu center. SCXRD confirmed these structural changes: after dosing, the framework forms the one-dimensional coordination polymer Cu(NH$_3$)$_4$(cyhdc), consistent with dissociation at the specified equatorial/axial sites (Fig. 28b). Adsorption/desorption isotherms show ~16 mmol g^{-1} at 298 K and 0.8 bar, reaching 17.5 mmol g^{-1} at

1.0 bar (Fig. 28c)—corresponding to ~4 NH_3 per Cu and comparable to the highest values reported for porous solids under similar conditions.[121,122] Importantly, Cu(NH$_3$)$_4$(cyhdc) reverts to Cu(cyhdc) upon desorption, demonstrating reversible dissociation–reassociation of metal–linker bonds and providing direct evidence of Cu(II)'s dynamic bonding nature during NH_3 sorption.

5.3.2 CO$_2$ adsorption *via* dynamic capping modulator exchange. Analogous to NH_3, CO_2 adsorption in certain MOFs proceeds through metal–linker dynamic bonding. The Farha group reported that CO_2 uptake in MOF-808 can be tuned by controlling the dynamicity of metal–modulator bonding.[123] MOF-808 consists of Zr–oxo clusters 6-connected to BTC linkers, with the remaining coordination sites capped by modulators. Dynamic exchange of these capping ligands transiently exposes Lewis-acidic Zr(IV) sites, generating binding centers for CO_2. The

This journal is © The Royal Society of Chemistry 2026
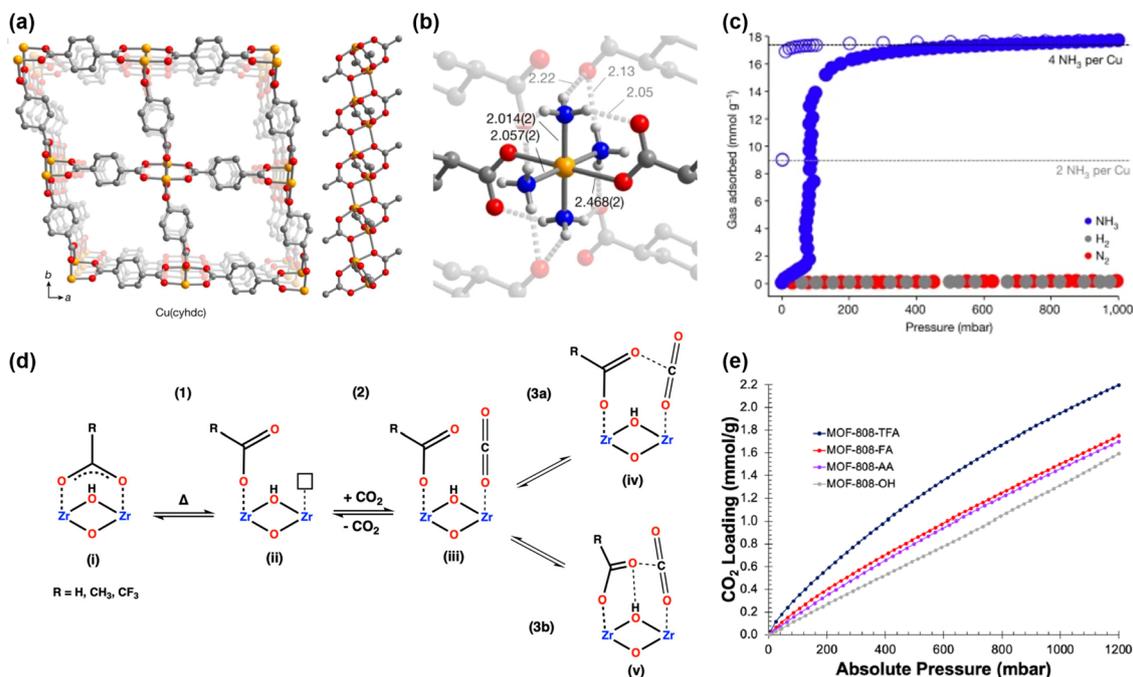
J. Mater. Chem. A, 2026, **14**, 9088–9114 | **9109**

Fig. 28 (a) Structure of Cu(cyhdc) showing rhombic channels defined by Cu–carboxylate paddlewheel vertices (left) and the one-dimensional paddlewheel chain motif (right). (b) Local Cu coordination in Cu(NH$_3$)$_4$(cyhdc) (Cu, orange; O, red; N, blue; C, grey; H, white; H omitted for clarity). (c) NH$_3$ adsorption/desorption isotherms at 298 K for Cu(cyhdc) (filled/open blue), with N$_2$ (red) and H$_2$ (grey) shown for comparison; dashed lines indicate capacities for two and four NH$_3$ per Cu site, respectively. Reproduced with permission from ref. 2, Copyright 2023, Springer Nature. (d) Hypothesized modulator/node dynamics in MOF-808. (e) CO$_2$ adsorption isotherms of MOF-808-X samples at 298.15 K. Reproduced with permission from ref. 123, Copyright 2023, American Chemical Society.

exchange propensity depends on the electronic character of the modulator: electron-withdrawing groups lower electron density at the coordinating O atoms and enhance bond dynamics, whereas electron-donating groups have the opposite effect. To demonstrate this property, MOF-808 was prepared with formic acid, acetic acid, and trifluoroacetic acid as capping modulators. The CF$_3$ group in trifluoroacetic acid withdraws electrons from the carboxylate O atoms, weakening the Zr–O bond and favoring a partially dissociated state; conversely, the CH$_3$ group in acetic acid donates electrons and suppresses partial dissociation (Fig. 28d). The resultingly formed transient OMSs act as CO$_2$ binding sites, with trifluoroacetic-acid-capped MOF-808 exhibiting the highest uptake among the tested modulators (Fig. 28e).

5.4 Stability enhancement achieved through dynamic metal–linker bonding

In various applications, most MOFs should overcome their stability issue, including structural degradation and loss of active sites during long-term use. To enhance stability, various strategies, for example, polymer incorporation, post-synthetic modifications, and rigidifying metal–linker coordination, have been explored to enhance stability; however, polymer incorporation and post-synthetic modifications often lead to the loss of surface areas and the change in the pore environments, and rigidifying metal–linker coordination reduces their dynamic natures, making the MOFs less suitable for applications that

need their dynamic bonding nature. Therefore, strategies for achieving a suitable balance between the stability and metal–linker dynamics have been developed by designing MOFs from birth: (i) introducing three-dimensional (3D) linkers, (ii) functionalizing organic linkers, and (iii) adjusting linker connectivity for varying structural topologies.

Introducing 3D linkers, in contrast to flat benzene-based linkers, increases framework rigidity through their bulkier geometries and thereby enhances structural stability. Farha and coworkers reported NU-2004, a MOF with a 3D linker (p-carborane-1,12-dicarboxylic acid), which has the same crystal structure as MIL-53.[124] The thermal stability examination conducted with temperature-variable PXRD measurements and N$_2$ adsorption–desorption isotherm demonstrates that the MOF maintains its structure well up to 400 °C. Employing temperature-variable SCXRD measurements, the structural dynamicity of MIL-53 with a 2D benzene linker, NU-2000 with a 3D aliphatic linker, and NU-2004 with a 3D aromatic linker was also tested. As a result, while MIL-53 showed 40% volume change upon the temperature variation, NU-2000 and NU-2004 showed only 6.6% and 1.4% volume changes, respectively, proving that increasing the rigidity of the metal–linker coordination decreases the structural flexibility in MOFs.

Functionalizing the organic linker with various substituents also provides a route for controlling the dynamicity and stability. Sugamata and colleagues first synthesized the Cu-paddlewheel MOF, named Cu-RCTC (R=H), employing the

9110 | J. Mater. Chem. A, 2026, 14, 9088–9114

This journal is © The Royal Society of Chemistry 2026

9,9′-(1,3-phenylene)bis(9H-carbazole-3,6-dicarboxylic acid) (H$_4$CTC) linker.[125] Then, in order to investigate the dynamicity depending on the functional groups, they synthesized a series of Cu-RCTC analogues, where R in the central phenylene ring was modified with H, Me, tBu, OMe, Br, or NO$_2$. Interestingly, the PXRD pattern of Cu–NO$_2$CTC became amorphous upon solvent removal, reflecting its low structural stability due to the strongly electron-withdrawing NO$_2$ group, which lowers the electron density at the linker's coordinating sites (oxygens in carboxylate) and thereby weakens metal–linker bonding. The H$_2$ uptake capacity in the order of tBu (2.45 wt%) > Me (2.25 wt%) > OMe (1.88 wt%) > Br (1.85 wt%) > NO$_2$ (1.00 wt%) also supports the relationship between the functional group and flexibility. Specifically, the higher flexibility enhances the stability of the activated MOF and thus increases its pore size and internal surface area, leading to higher uptake of H$_2$ molecules.

Finally, varying the framework topology by increasing linker connectivity has also been considered an effective strategy to enhance MOF stability. For instance, Bůžek and colleagues examined the stability of four Zr-based MOFs (UiO-66, MOF-808, MIP-200, and PCN-222), which are constructed from the ditopic, tritopic, and tetratopic linkers, respectively, to vary the connectivity and net topology.[126] They examined their structural stability under various pH conditions by evaluating the degradation, monitoring the linker release amounts, N$_2$ sorption isotherms, and PXRD patterns. As a result, MIP-200 and PCN-222, both with tetratopic linkers, exhibit higher stability than UiO-66 and MOF-808 with ditopic and tritopic linkers, respectively. This result indicates that higher connectivity can enhance the MOF stability. Although this topology-dependent stability was elucidated just by using the rigid Zr–carboxylate coordination bond, this concept might be expanded to other hemilabile MOFs, providing an insight for designing MOFs.

6 Summary and outlook

This review reframes MOFs as responsive coordination networks rather than static scaffolds. Across chemistries and length scales, coordination links at both OMSs and within metal–linker junctions populate equilibria between associated and partially dissociated states; these populations are tunable based on temperature, light, guest basicity, spatial confinedness, and crystal dimension—without loss of long-range order.

Through this dynamic lens, function follows. Reversible exchange at OMSs enables low-energy activation and governs substrate access during catalysis, while cooperative sorption emerges when bond populations shift collectively under adsorbates. Within the lattice backbone, transient metal–linker dissociation creates hemilabile environments that open catalytic pathways at nominally saturated nodes and mediate structure-preserving reorganization into transiently non-crystalline states.

Despite its broad applicability to catalysis, gas sorption, and delivery, the mechanism study of dynamic coordination-bondings in MOFs remains challenging. Factors governing coordination strength at metal–guest interfaces are still underexplored, in part due to the limitation in tools for measuring and comparing energetics under operando conditions. Progress will benefit from spectroscopy with higher spatial and temporal resolution, integrated with variable-temperature/variable-pressure protocols, to directly quantify bond dynamicities and exchange rates. Complementary computational simulations—ranging from excited-state dynamics to enhanced-sampling molecular dynamics and free-energy profiling—are essential to resolve pathways and kinetics and to link spectroscopic observables with the mechanism.

Finally, dynamic coordination has largely been pursued via synthesis-first, characterize-later workflows. As chemical space continues to expand, exclusive reliance on experimental intuition can be increasingly inefficient. Data-centric approaches and machine learning may offer a route to design and pre-screen frameworks with targeted dynamicity, predict tunable levers (metal identity, linker electronics/sterics, pore architecture, and crystal size), and propose feasible synthetic routes. By leveraging computational approaches to control framework dynamicity and identify viable synthetic routes, these strategies can substantially reduce experimental trial-and-error and accelerate the discovery of MOFs with enhanced applicability in areas such as catalysis and gas sorption. By predicting structures with controlled dynamicity and identifying feasible synthetic routes, such approaches have the potential to reduce experimental effort and accelerate the discovery of MOFs with improved applicability.

Author contributions

S. H. P., B. J. K., J. C., and I. K. wrote the original draft. S. H. P. visualized the work, including schematic illustrations, and conceptualized the study. N. C. J. supervised all the papers.

Conflicts of interest

There are no conflicts to declare.

Data availability

No primary research results, software or code have been included and no new data were generated or analysed as part of this review.

Acknowledgements

Notes and references

1 W. Fan, X. Zhang, Z. Kang, X. Liu and D. Sun, Coord. Chem. Rev., 2021, 443, 213968.

This journal is © The Royal Society of Chemistry 2026

J. Mater. Chem. A, 2026, 14, 9088–9114 | 9111

2   B. E. R. Snyder, A. B. Turkiewicz, H. Furukawa, M. V. Paley, E. O. Velasquez, M. N. Dods and J. R. Long, *Nature*, 2023, **613**, 287–291.

3   J. H. Choe, H. Kim, H. Yun, J. F. Kurisingal, N. Kim, D. Lee, Y. H. Lee and C. S. Hong, *J. Am. Chem. Soc.*, 2024, **146**, 19337–19349.

4   C. Y. Heo, M. L. Díaz-Ramírez, S. H. Park, M. Kang, C. S. Hong and N. C. Jeong, *ACS Appl. Mater. Interfaces*, 2024, **16**, 9068–9077.

5   S. H. Park, H. M. Kim, M. L. Díaz-Ramírez, S. Lee and N. C. Jeong, *Chem. Commun.*, 2024, **60**, 14577–14580.

6   Y.-C. Wang, S.-C. Yang, C.-H. Shen, T.-H. Yang and C.-W. Kung, *CrystEngComm*, 2025, **27**, 5830–5840.

7   K. Yue, R. Lu, M. Gao, F. Song, Y. Dai, C. Xia, B. Mei, H. Dong, R. Qi, D. Zhang, J. Zhang, Z. Wang, F. Huang, B. Y. Xia and Y. Yan, *Science*, 2025, **388**, 430–436.

8   Z. Hu and D. Zhao, *CrystEngComm*, 2017, **19**, 4066–4081.

9   E. Pérez-Mayoral, Z. Musilová, B. Gil, B. Marszalek, M. Položij, P. Nachtigall and J. Čejka, *Dalton Trans.*, 2012, **41**, 4036–4044.

10 B. J. Kim, S. H. Park, M. L. Díaz-Ramírez and N. C. Jeong, *Chem. Commun.*, 2025, **61**, 3582–3600.

11 M. Park, H. Ju, J. Oh, K. Park, H. Lim, S. M. Yoon and I. Song, *Nat. Commun.*, 2025, **16**, 1316.

12 B. Thomas, S. Basak, Q. Smith, M. Yan and A. J. Morris, *J. Am. Chem. Soc.*, 2025, **147**, 33655–33665.

13 Y.-M. Jo, D.-H. Kim, J. Wang, J. J. Oppenheim and M. Dincă, *J. Am. Chem. Soc.*, 2024, **146**, 20213–20220.

14 K. Jin, D. Moon, Y.-P. Chen and J. Park, *Adv. Mater.*, 2024, **36**, 2309570.

15 Z. Han, K.-Y. Wang, R.-R. Liang, Y. Guo, Y. Yang, M. Wang, Y. Mao, J. Huo, W. Shi and H.-C. Zhou, *J. Am. Chem. Soc.*, 2025, **147**, 3866–3873.

16 W. Jang, H. Yoo, D. Shin, S. Noh and J. Y. Kim, *Nat. Commun.*, 2025, **16**, 385.

17 H. Kim, S. Yang, S. R. Rao, S. Narayanan, E. A. Kapustin, H. Furukawa, A. S. Umans, O. M. Yaghi and E. N. Wang, *Science*, 2017, **356**, 430–434.

18 N. Hanikel, X. Pei, S. Chheda, H. Lyu, W. Jeong, J. Sauer, L. Gagliardi and O. M. Yaghi, *Science*, 2021, **374**, 454–459.

19 J. Bae, S. H. Park, D. Moon and N. C. Jeong, *Commun. Chem.*, 2022, **5**, 51.

20 M. S. Kang, I. Heo, S. H. Park, J. Bae, S. Kim, G. Kim, B.-H. Kim, N. C. Jeong and W. C. Yoo, *Nat. Commun.*, 2024, **15**, 9793.

21 J. L. Obeso, M. T. Huxley, C. Leyva, J. Gabriel Flores, N. Martín-Guaregua, M. Viniegra, J. Aguilar-Pliego, J. Antonio de los Reyes, I. A. Ibarra and R. A. Peralta, *Coord. Chem. Rev.*, 2023, **496**, 215403.

22 E. Svensson Grape, A. M. Davenport and C. K. Brozek, *Dalton Trans.*, 2024, **53**, 1935–1941.

23 O. M. Yaghi, M. O'Keeffe, N. W. Ockwig, H. K. Chae, M. Eddaoudi and J. Kim, *Nature*, 2003, **423**, 705–714.

24 V. Guillerm and M. Eddaoudi, *Acc. Chem. Res.*, 2021, **54**, 3298–3312.

25 H.-Y. Li, X.-J. Kong, S.-D. Han, J. Pang, T. He, G.-M. Wang and X.-H. Bu, *Chem. Soc. Rev.*, 2024, **53**, 5626–5676.

26 H. Xie, K. O. Kirlikovali, Z. Chen, K. B. Idrees, T. Islamoglu and O. K. Farha, *J. Mater. Chem. A*, 2024, **12**, 6399–6404.

27 K. Leus, I. Muylaert, M. Vandichel, G. B. Marin, M. Waroquier, V. Van Speybroeck and P. Van Der Voort, *Chem. Commun.*, 2010, **46**, 5085–5087.

28 J. Hajek, B. Bueken, M. Waroquier, D. De Vos and V. Van Speybroeck, *ChemCatChem*, 2017, **9**, 2203–2210.

29 P. Lyu, A. M. Wright, A. López-Olvera, P. G. M. Mileo, J. A. Zárate, E. Martínez-Ahumada, V. Martis, D. R. Williams, M. Dincă, I. A. Ibarra and G. Maurin, *Chem. Mater.*, 2021, **33**, 6186–6192.

30 R. Ma, C. Qiao, L. Xia, Z. Xia, Q. Yang, Y. Xu, G. Xie, S. Chen and S. Gao, *Inorg. Chem.*, 2022, **61**, 7484–7496.

31 R. A. Peralta, M. T. Huxley, P. Lyu, M. L. Díaz-Ramírez, S. H. Park, J. L. Obeso, C. Leyva, C. Y. Heo, S. Jang, J. H. Kwak, G. Maurin, I. A. Ibarra and N. C. Jeong, *ACS Appl. Mater. Interfaces*, 2023, **15**, 1410–1417.

32 S. H. Park, R. A. Peralta, D. Moon and N. C. Jeong, *J. Mater. Chem. A*, 2022, **10**, 23499–23508.

33 H. K. Kim, W. S. Yun, M.-B. Kim, J. Y. Kim, Y.-S. Bae, J. Lee and N. C. Jeong, *J. Am. Chem. Soc.*, 2015, **137**, 10009–10015.

34 J. Bae, J. S. Choi, S. Hwang, W. S. Yun, D. Song, J. Lee and N. C. Jeong, *ACS Appl. Mater. Interfaces*, 2017, **9**, 24743–24752.

35 J. S. Choi, J. Bae, E. J. Lee and N. C. Jeong, *Inorg. Chem.*, 2018, **57**, 5225–5231.

36 J. Bae, E. J. Lee and N. C. Jeong, *Chem. Commun.*, 2018, **54**, 6458–6471.

37 J. Bae, C. Y. Lee and N. C. Jeong, *Bull. Korean Chem. Soc.*, 2021, **42**, 658–666.

38 H. I. Song, J. Bae, E. J. Lee, K. O. Kirlikovali, O. K. Farha and N. C. Jeong, *J. Phys. Chem. C*, 2020, **124**, 13187–13195.

39 M. L. Díaz-Ramírez, S. H. Park, M. Rivera-Almazo, E. Medel, R. A. Peralta, I. A. Ibarra, R. Vargas, J. Garza and N. C. Jeong, *Chem. Sci.*, 2025, **16**, 2581–2588.

40 J. Espín, L. Garzón-Tovar, A. Carné-Sánchez, I. Imaz and D. Maspoch, *ACS Appl. Mater. Interfaces*, 2018, **10**, 9555–9562.

41 D. S. Choi, D. W. Kim, D. W. Kang, M. Kang, Y. S. Chae and C. S. Hong, *J. Mater. Chem. A*, 2021, **9**, 21424–21428.

42 J. H. Choe, H. Kim, M. Kang, H. Yun, S. Y. Kim, S. M. Lee and C. S. Hong, *J. Am. Chem. Soc.*, 2022, **144**, 10309–10319.

43 J. H. Choe, H. Kim, H. Yun, M. Kang, S. Park, S. Yu and C. S. Hong, *J. Am. Chem. Soc.*, 2024, **146**, 646–659.

44 J. F. Kurisingal, J. H. Choe, H. Kim, J. Youn, G. Cheon and C. S. Hong, *Bull. Korean Chem. Soc.*, 2024, **45**, 675–688.

45 J. L. Obeso, D. R. Amaro, C. V. Flores, A. Gutiérrez-Alejandre, R. A. Peralta, C. Leyva and I. A. Ibarra, *Coord. Chem. Rev.*, 2023, **485**, 215135.

46 J. L. Obeso, A. López-Olvera, C. V. Flores, R. A. Peralta, I. A. Ibarra and C. Leyva, *Chem. Commun.*, 2023, **59**, 3273–3276.

47 R. A. Peralta and I. A. Ibarra, *CrystEngComm*, 2024, **26**, 6100–6107.

48 J. Fonseca, T. Gong, L. Jiao and H.-L. Jiang, *J. Mater. Chem. A*, 2021, **9**, 10562–10611.

49 N. Ma and S. Horike, *Chem. Rev.*, 2022, **122**, 4163–4203.

9112 | *J. Mater. Chem. A*, 2026, **14**, 9088–9114

This journal is © The Royal Society of Chemistry 2026

50 M. Kim, Y. Lee and H. R. Moon, *Acc. Chem. Res.*, 2024, **57**, 2347–2357.

51 S. Sen, N. Hosono, J.-J. Zheng, S. Kusaka, R. Matsuda, S. Sakaki and S. Kitagawa, *J. Am. Chem. Soc.*, 2017, **139**, 18313–18321.

52 H. Sato, W. Kosaka, R. Matsuda, A. Hori, Y. Hijikata, R. V. Belosludov, S. Sakaki, M. Takata and S. Kitagawa, *Science*, 2014, **343**, 167–170.

53 Y. Chen, Y. Du, P. Liu, J. Yang, L. Li and J. Li, *Environ. Sci. Technol.*, 2020, **54**, 3636–3642.

54 Ü. Kökçam-Demir, A. Goldman, L. Esrafili, M. Gharib, A. Morsali, O. Weingart and C. Janiak, *Chem. Soc. Rev.*, 2020, **49**, 2751–2798.

55 L. Helm and A. E. Merbach, *Chem. Rev.*, 2005, **105**, 1923–1960.

56 N. M. Shavaleev, S. V. Eliseeva, R. Scopelliti and J.-C. G. Bünzli, *Inorg. Chem.*, 2015, **54**, 9166–9173.

57 M. R. Friedfeld, H. Zhong, R. T. Ruck, M. Shevlin and P. J. Chirik, *Science*, 2018, **360**, 888–893.

58 N. Shida, Y. Imada, S. Nagahara, Y. Okada and K. Chiba, *Commun. Chem.*, 2019, **2**, 24.

59 J. Li, C.-Y. Huang, M. Ataya, R. Z. Khaliullin and C.-J. Li, *Nat. Commun.*, 2021, **12**, 4970.

60 W. M. Haynes, *CRC Handbook of Chemistry and Physics*, CRC Press, Boca Raton, 97th edn, 2016.

61 R. M. Badger, *J. Chem. Phys.*, 1934, **2**, 128–131.

62 S. Bode, L. Zedler, F. H. Schacher, B. Dietzek, M. Schmitt, J. Popp, M. D. Hager and U. S. Schubert, *Adv. Mater.*, 2013, **25**, 1634–1638.

63 J. Hou, M. L. Ríos Gómez, A. Krajnc, A. McCaul, S. Li, A. M. Bumstead, A. F. Sapnik, Z. Deng, R. Lin, P. A. Chater, D. S. Keeble, D. A. Keen, D. Appadoo, B. Chan, V. Chen, G. Mali and T. D. Bennett, *J. Am. Chem. Soc.*, 2020, **142**, 3880–3890.

64 A. B. Andreeva, K. N. Le, L. Chen, M. E. Kellman, C. H. Hendon and C. K. Brozek, *J. Am. Chem. Soc.*, 2020, **142**, 19291–19299.

65 A. B. Andreeva, K. N. Le, K. Kadota, S. Horike, C. H. Hendon and C. K. Brozek, *Chem. Mater.*, 2021, **33**, 8534–8545.

66 Q. Ye, D. R. Cairnie, D. Troya, N. Kumar, X. Yang and A. J. Morris, *J. Am. Chem. Soc.*, 2024, **146**, 101–105.

67 K. Fabrizio, A. B. Andreeva, K. Kadota, A. J. Morris and C. K. Brozek, *Chem. Commun.*, 2023, **59**, 1309–1312.

68 K. Fabrizio and C. K. Brozek, *Nano Lett.*, 2023, **23**, 925–930.

69 A. J. Howarth, A. W. Peters, N. A. Vermeulen, T. C. Wang, J. T. Hupp and O. K. Farha, *Chem. Mater.*, 2017, **29**, 26–39.

70 X. Zhang, Z. Chen, X. Liu, S. L. Hanna, X. Wang, R. Taheri-Ledari, A. Maleki, P. Li and O. K. Farha, *Chem. Soc. Rev.*, 2020, **49**, 7406–7427.

71 B. F. Abrahams, B. F. Hoskins, D. M. Michail and R. Robson, *Nature*, 1994, **369**, 727–729.

72 G. Ferey, C. Mellot-Draznieks, C. Serre, F. Millange, J. Dutour, S. Surble and I. Margiolaki, *Science*, 2005, **309**, 2040–2042.

73 J. H. Cavka, S. Jakobsen, U. Olsbye, N. Guillou, C. Lamberti, S. Bordiga and K. P. Lillerud, *J. Am. Chem. Soc.*, 2008, **130**, 13850–13851.

74 H. Li, M. Eddaoudi, M. O'Keeffe and O. M. Yaghi, *Nature*, 1999, **402**, 276–279.

75 A. P. Nelson, O. K. Farha, K. L. Mulfort and J. T. Hupp, *J. Am. Chem. Soc.*, 2009, **131**, 458–460.

76 D. S. Choi, D. W. Kim, J.-H. Lee, Y. S. Chae, D. W. Kang and C. S. Hong, *ACS Appl. Mater. Interfaces*, 2021, **13**, 38358–38364.

77 Y. Seok Chae, S. Park, D. Won Kang, D. Won Kim, M. Kang, D. San Choi, J. Hyeak Choe and C. Seop Hong, *Chem. Eng. J.*, 2022, **433**, 133856.

78 B. Dinakar, A. C. Forse, H. Z. H. Jiang, Z. Zhu, J.-H. Lee, E. J. Kim, S. T. Parker, C. J. Pollak, R. L. Siegelman, P. J. Milner, J. A. Reimer and J. R. Long, *J. Am. Chem. Soc.*, 2021, **143**, 15258–15270.

79 S. T. Parker, A. Smith, A. C. Forse, W.-C. Liao, F. Brown-Altvater, R. L. Siegelman, E. J. Kim, N. A. Zill, W. Zhang, J. B. Neaton, J. A. Reimer and J. R. Long, *J. Am. Chem. Soc.*, 2022, **144**, 19849–19860.

80 R. L. Siegelman, J. A. Thompson, J. A. Mason, T. M. McDonald and J. R. Long, *Chem. Sci.*, 2022, **13**, 11772–11784.

81 T. Lei, D. Wang, X. Yu, S. Ma, W. Zhao, C. Cui, J. Meng, S. Tao and D. Guan, *Nature*, 2023, **622**, 514–520.

82 K. Rennert, F. Errickson, B. C. Prest, L. Rennels, R. G. Newell, W. Pizer, C. Kingdon, J. Wingenroth, R. Cooke, B. Parthum, D. Smith, K. Cromar, D. Diaz, F. C. Moore, U. K. Müller, R. J. Plevin, A. E. Raftery, H. Ševčíková, H. Sheets, J. H. Stock, T. Tan, M. Watson, T. E. Wong and D. Anthoff, *Nature*, 2022, **610**, 687–692.

83 P. Stegmann, V. Daioglou, M. Londo, D. P. van Vuuren and M. Junginger, *Nature*, 2022, **612**, 272–276.

84 J. R. Zondervan, R. G. Hilton, M. Dellinger, F. J. Clubb, T. Roylands and M. Ogrič, *Nature*, 2023, **623**, 329–333.

85 P. G. Boyd, A. Chidambaram, E. García-Díez, C. P. Ireland, T. D. Daff, R. Bounds, A. Gładysiak, P. Schouwink, S. M. Moosavi, M. M. Maroto-Valer, J. A. Reimer, J. A. R. Navarro, T. K. Woo, S. Garcia, K. C. Stylianou and B. Smit, *Nature*, 2019, **576**, 253–256.

86 R. C. Rohde, K. M. Carsch, M. N. Dods, H. Z. H. Jiang, A. R. McIsaac, R. A. Klein, H. Kwon, S. L. Karstens, Y. Wang, A. J. Huang, J. W. Taylor, Y. Yabuuchi, N. V. Tkachenko, K. R. Meihaus, H. Furukawa, D. R. Yahne, K. E. Engler, K. C. Bustillo, A. M. Minor, J. A. Reimer, M. Head-Gordon, C. M. Brown and J. R. Long, *Science*, 2024, **386**, 814–819.

87 Z. Zhou, T. Ma, H. Zhang, S. Chheda, H. Li, K. Wang, S. Ehrling, R. Giovine, C. Li, A. H. Alawadhi, M. M. Abduljawad, M. O. Alawad, L. Gagliardi, J. Sauer and O. M. Yaghi, *Nature*, 2024, **635**, 96–101.

88 T. M. McDonald, J. A. Mason, X. Kong, E. D. Bloch, D. Gygi, A. Dani, V. Crocellà, F. Giordanino, S. O. Odoh, W. S. Drisdell, B. Vlaisavljevich, A. L. Dzubak, R. Poloni, S. K. Schnell, N. Planas, K. Lee, T. Pascal, L. F. Wan, D. Prendergast, J. B. Neaton, B. Smit, J. B. Kortright, L. Gagliardi, S. Bordiga, J. A. Reimer and J. R. Long, *Nature*, 2015, **519**, 303–308.

This journal is © The Royal Society of Chemistry 2026

J. Mater. Chem. A, 2026, **14**, 9088–9114 | 9113

89 Z. Zhu, H. Tsai, S. T. Parker, J.-H. Lee, Y. Yabuuchi, H. Z. H. Jiang, Y. Wang, S. Xiong, A. C. Forse, B. Dinakar, A. Huang, C. Dun, P. J. Milner, A. Smith, P. Guimarães Martins, K. R. Meihaus, J. J. Urban, J. A. Reimer, J. B. Neaton and J. R. Long, *J. Am. Chem. Soc.*, 2024, **146**, 6072–6083.

90 X. Gui, Z. Tang and W. Fei, *J. Chem. Eng. Data*, 2010, **55**, 3736–3741.

91 J. C. Fisher, II, R. V. Siriwardane and R. W. Stevens, Jr., *Ind. Eng. Chem. Res.*, 2012, **51**, 5273–5281.

92 Z. Zhu, S. T. Parker, A. C. Forse, J.-H. Lee, R. L. Siegelman, P. J. Milner, H. Tsai, M. Ye, S. Xiong, M. V. Paley, A. A. Uliana, J. Oktawiec, B. Dinakar, S. A. Didas, K. R. Meihaus, J. A. Reimer, J. B. Neaton and J. R. Long, *J. Am. Chem. Soc.*, 2023, **145**, 17151–17163.

93 C. M. McGuirk, R. L. Siegelman, W. S. Drisdell, T. Runčevski, P. J. Milner, J. Oktawiec, L. F. Wan, G. M. Su, H. Z. H. Jiang, D. A. Reed, M. I. Gonzalez, D. Prendergast and J. R. Long, *Nat. Commun.*, 2018, **9**, 5133.

94 X. Chen, B.-X. Shen, H. Sun, G.-X. Zhan and Z.-Z. Huo, *Ind. Eng. Chem. Res.*, 2017, **56**, 6499–6507.

95 R. A. Peralta, P. Lyu, A. López-Olvera, J. L. Obeso, C. Leyva, N. C. Jeong, I. A. Ibarra and G. Maurin, *Angew. Chem., Int. Ed.*, 2022, **61**, e202210857.

96 M. Pera-Titus, *Chem. Rev.*, 2014, **114**, 1413–1492.

97 Y. Wang, T. Luo, B. Elander, Y. Mu, D. Wang, U. Mohanty and J. L. Bao, *ACS Appl. Mater. Interfaces*, 2023, **15**, 21659–21678.

98 M. Kalaj, K. C. Bentz, S. Ayala, Jr., J. M. Palomba, K. S. Barcus, Y. Katayama and S. M. Cohen, *Chem. Rev.*, 2020, **120**, 8267–8302.

99 M. Pérez-Miana, J. M. Luque-Alled, Á. Mayoral, Í. Martínez-Visus, A. B. Foster, P. M. Budd and J. Coronas, *Angew. Chem., Int. Ed.*, 2025, **64**, e202420879.

100 B. Yeskendir, J.-P. Dacquin, Y. Lorgouilloux, C. Courtois, S. Royer and J. Dhainaut, *Mater. Adv.*, 2021, **2**, 7139–7186.

101 Z. Wang, L. Liu, Z. Li, N. Goyal, T. Du, J. He and G. K. Li, *Energy Fuels*, 2022, **36**, 2927–2944.

102 S. Naskar, D. Fan, A. Ghoufi and G. Maurin, *Chem. Sci.*, 2023, **14**, 10435–10445.

103 C. Wu, L.-Y. Chou, L. Long, X. Si, W.-S. Lo, C.-K. Tsung and T. Li, *ACS Appl. Mater. Interfaces*, 2019, **11**, 35820–35826.

104 M. Choe, J. Y. Koo, I. Park, H. Ohtsu, J. H. Shim, H. C. Choi and S. S. Park, *J. Am. Chem. Soc.*, 2022, **144**, 16726–16731.

105 A. Fuchs, F. Knechtel, H. Wang, Z. Ji, S. Wuttke, O. M. Yaghi and E. Ploetz, *J. Am. Chem. Soc.*, 2023, **145**, 14324–14334.

106 L. Luo, L. Hou, X. Cui, P. Zhan, P. He, C. Dai, R. Li, J. Dong, Y. Zou, G. Liu, Y. Liu and J. Zheng, *Nat. Commun.*, 2024, **15**, 3618.

107 J. Ding, T. Du, E. H. Thomsen, D. Andresen, M. R. Fischer, A. K. Møller, A. R. Petersen, A. K. Pedersen, L. R. Jensen, S. Wang and M. M. Smedskjaer, *Advanced Science*, 2024, **11**, 2306698.

108 R. Banerjee, A. Phan, B. Wang, C. Knobler, H. Furukawa, M. O'Keeffe and O. M. Yaghi, *Science*, 2008, **319**, 939–943.

109 K. Noh, J. Lee and J. Kim, *Isr. J. Chem.*, 2018, **58**, 1075–1088.

110 J. Song, L. Frentzel-Beyme, R. Pallach, P. Kolodzeiski, A. Koutsianos, W.-L. Xue, R. Schmid and S. Henke, *J. Am. Chem. Soc.*, 2023, **145**, 9273–9284.

111 A. M. Bumstead, M. L. Ríos Gómez, M. F. Thorne, A. F. Sapnik, L. Longley, J. M. Tuffnell, D. S. Keeble, D. A. Keen and T. D. Bennett, *CrystEngComm*, 2020, **22**, 3627–3637.

112 T. D. Bennett, Y. Yue, P. Li, A. Qiao, H. Tao, N. G. Greaves, T. Richards, G. I. Lampronti, S. A. T. Redfern, F. Blanc, O. K. Farha, J. T. Hupp, A. K. Cheetham and D. A. Keen, *J. Am. Chem. Soc.*, 2016, **138**, 3484–3492.

113 L. León-Alcaide, R. S. Christensen, D. A. Keen, J. L. Jordá, I. Brotons-Alcázar, A. Forment-Aliaga and G. Mínguez Espallargas, *J. Am. Chem. Soc.*, 2023, **145**, 11258–11264.

114 T. D. Bennett, J.-C. Tan, Y. Yue, E. Baxter, C. Ducati, N. J. Terrill, H. H. M. Yeung, Z. Zhou, W. Chen, S. Henke, A. K. Cheetham and G. N. Greaves, *Nat. Commun.*, 2015, **6**, 8079.

115 M. Kim, H.-S. Lee, D.-H. Seo, S. J. Cho, E.-C. Jeon and H. R. Moon, *Nat. Commun.*, 2024, **15**, 1174.

116 S. Li, R. Limbach, L. Longley, A. A. Shirzadi, J. C. Walmsley, D. N. Johnstone, P. A. Midgley, L. Wondraczek and T. D. Bennett, *J. Am. Chem. Soc.*, 2019, **141**, 1027–1034.

117 Z. Yu, L. Tang, N. Ma, S. Horike and W. Chen, *Coord. Chem. Rev.*, 2022, **469**, 214646.

118 T. D. Bennett, T. K. Todorova, E. F. Baxter, D. G. Reid, C. Gervais, B. Bueken, B. Van de Voorde, D. De Vos, D. A. Keen and C. Mellot-Draznieks, *Phys. Chem. Chem. Phys.*, 2016, **18**, 2192–2201.

119 Z. Su, Y.-R. Miao, G. Zhang, J. T. Miller and K. S. Suslick, *Chem. Sci.*, 2017, **8**, 8004–8011.

120 T. Kurihara, K. Ohara, K. Kadota, H. Izu, Y. Nishiyama, M. Mizuno and S. Horike, *Inorg. Chem.*, 2022, **61**, 16103–16109.

121 A. J. Rieth, A. M. Wright and M. Dincă, *Nat. Rev. Mater.*, 2019, **4**, 708–725.

122 D. W. Kim, D. W. Kang, M. Kang, J.-H. Lee, J. H. Choe, Y. S. Chae, D. S. Choi, H. Yun and C. S. Hong, *Angew. Chem., Int. Ed.*, 2020, **59**, 22531–22536.

123 T. M. Rayder, F. Formalik, S. M. Vornholt, H. Frank, S. Lee, M. Alzayer, Z. Chen, D. Sengupta, T. Islamoglu, F. Paesani, K. W. Chapman, R. Q. Snurr and O. K. Farha, *J. Am. Chem. Soc.*, 2023, **145**, 11195–11205.

124 K. B. Idrees, K. O. Kirlikovali, C. Setter, H. Xie, H. Brand, B. Lal, F. Sha, C. S. Smoljan, X. Wang, T. Islamoglu, L. K. Macreadie and O. K. Farha, *J. Am. Chem. Soc.*, 2023, **145**, 23433–23441.

125 K. Sugamata, A. Shirai and M. Minoura, *Chem.–Eur. J.*, 2023, **29**, e202203442.

126 D. Bůžek, J. Hynek, M. Kloda, V. Zlámalová, P. Bezdička, S. Adamec, K. Lang and J. Demel, *Inorg. Chem. Front.*, 2024, **11**, 5319–5335.

9114 | *J. Mater. Chem. A*, 2026, **14**, 9088–9114

This journal is © The Royal Society of Chemistry 2026